UNIVERSITY OF TARTU
Faculty of Science and Technology
Institute of Chemistry

Dmytro Danilian

X-RAY PHOTOELECTRON SPECTROSCOPY STUDIES OF CARBON-BASED ELECTROCATALYTIC MATERIALS

Master's Thesis
(30 ECTS in Applied Measurement Science)

Supervisors:

Arvo Kikas
Vambola Kisand
Laboratory of X-ray spectroscopy
Institute of Physics
University of Tartu

Kaido Tammeveski
Chair of Colloid and Environmental Chemistry
Institute of Chemistry
University of Tartu

Tartu 2020

TABLE OF CONTENTS

ABBREVIATIONS

BE	Binding energy
CDC	Carbide-derived carbon
DCDA	Dicyandiamide
ESCA	Electron Spectroscopy for Chemical Analysis
HAXPES.	Hard X-ray PhotoElectron Spectroscopy
LEED	Low energy electron diffraction
LOD	Limit of detection
MNC	Metal-nitrogen-carbon
MR	Methylresorcinol
ORR	Oxygen reduction reaction
IMFP	Inelastic mean free path
PEM	Polymer electrolyte membrane
PES	Photoelectron spectroscopy
UPS	Ultraviolet Photoelectron Spectroscopy
XPS	X-ray Photoelectron Spectroscopy

INTRODUCTION

One of the key challenges of present times is the development of renewable energy carriers to replace today's fossil emissions cycle. Renewable power generated by hydrogen fuel cells is a potential alternative solution to fossil fuel consumption [1]. Fuel cells play a significant role in the hydrogen energy cycle, offering a way of producing clean-energy, with the main obstacle to implement sustainable and efficient low-temperature fuel cell systems based on cathodic oxygen reduction reaction (ORR). The main issues currently emerge, however, from the high cost of electrocatalysts used for ORR. Historically, high-area carbon materials supported platinum nanoparticles (Pt/C) are used as a catalyst for fuel cells with low temperatures [2].

Rigorous work was directed at developing cost-effective ORR electrocatalysts. Since Pt-based electrocatalysts suffer high costs of Pt and problems of deactivation due to CO and methanol poisoning, research has focused on the development of non-noble metal or completely metal-free catalysts [3]. The best performance in catalyzing the ORR has been shown by transition-metal and nitrogen co-doped carbon materials, obtained through the thermal treatment of metal, nitrogen and carbon precursors. Many such approaches even exceed Pt/C benchmark catalysts [4].

Aim of the study is to determine the surface composition of electrocatalysts by X-ray photoelectron spectroscopy (XPS).

Objects of study of this thesis are the carbon-based electrocatalysts prepared by Kaido Tammeveski's research group. More precisely, surface states and electronic structure of two series of prepared materials are studied. The first series of metal-nitrogen-carbon (MNC) catalysts were prepared using 5-methylresorcinol (5MR) and dicyandiamide (DCDA) as the precursors and doped with Fe and Co. The same materials were studied with and without acid treatment during production. The second series of studied samples were catalysts based on carbide-derived carbon (CDC), samples were milled in different conditions.

XPS had been used for characterization of these samples. This method allows determining the chemical and electronic structure of the surface layer of material. In this master's thesis, XPS has been used as an analytical tool to obtain information about the relative concentrations of elements and compounds that are present on or near the surface.

1. LITERATURE OVERVIEW

1.1 Photoemission spectroscopy (PES)

The photoelectric effect is a crucial way of understanding PES principles. The photoelectric effect shows that electrons can be driven off the solid surface by electromagnetic radiation. The electrons that have been expelled are called photoelectrons.

When the electron in the sample receives a photon incident, the photon is absorbed, and its energy is used to free that electron from bound atomic state. The energy needed to detach an electron from the atom is called the binding energy of an electron in the atom. Core electrons have higher binding energies than valence electrons as they are nearest to the atom nucleus and therefore have a higher affinity to the nucleus. Electron will be rejected from the atoms as the energy of the emitted photons is greater than the electrons' binding energy (formula 1.1):

$$E_k = hv - E_B - W, \qquad (1.1)$$

where E_k is the kinetic energy, h is the Planck's constant, v is the ionized light frequency, and E_B is the electron-binding with energy ionization energy, and W is the work function [5].

Figure 1.1 depicts the photoemission process, where the electron from the K-shell is expelled from the atom.

The photoelectron spectrum closely reproduces the electronic structure of the chemical elements, as all electrons that have a lower binding energy than photon energy are present in the spectrum.

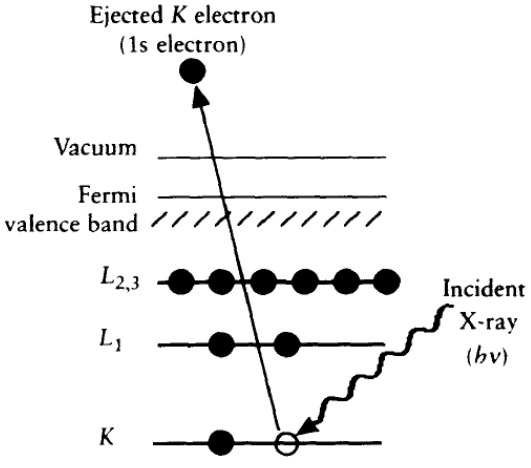

Figure 1.1. Schematic diagram of the XPS process, showing photoionization of an atom by the ejection of a 1s electron [5].

PES can be categorized into Ultraviolet Photoelectron Spectroscopy (UPS), X-ray Photoelectron Spectroscopy (XPS) and Hard X-ray PhotoElectron Spectroscopy (HAXPES) according to the energy of ionization source [3].

1.1.1 X-ray photoelectron spectroscopy

XPS is a technique for the study of surface chemistry in a material, also known as electron spectroscopy for chemical analysis (ESCA). The elemental composition, chemical state, and electronic state of elements in a substance can be determined by XPS. XPS spectra are obtained when a solid surface is irradiated by X-ray radiation, while the kinetic energy and electrons released from the top 1-10 nm of the sample being studied are concurrently determined. By counting electron expelled through a range of electron kinetic energies, a photoelectron spectrum is registered. Peaks occur in the spectrum of atoms, which emit electrons with a specific characteristic energy. The frequency and intensity of the photoelectron peaks allow all surface elements to be identified and quantified (except hydrogen) [6]. For XPS, X-ray tubes with photon energy 1000-1500 eV are mainly used as photon sources. XPS will eject electrons out of the core and valence levels.

1.2 Surface sensitivity

1.2.1 Surface

Figure 1.2 shows that a surface layer (≈1 nm) depending on the material is defined as up to three atomic layers in thickness. The layers until about 10 nm are considered to be ultra-thin films and thin films up to around 1 μm. The rest of the solid is considered bulk material. This description is not universal, though, and the distinction between the types of layers that vary depending on the material and its application.

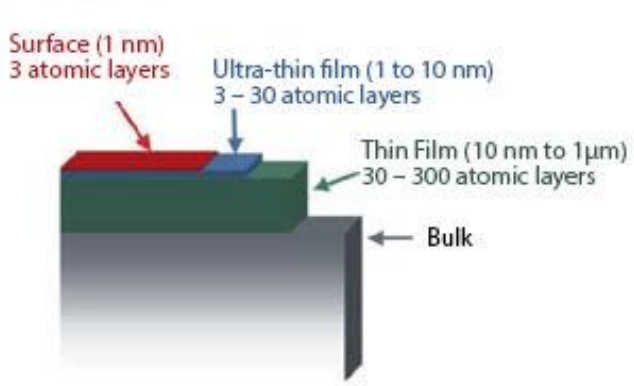

Figure 1.2. Surface characterization [7].

The surface reflects a discontinuity between one phase and another, which results in varying surface physical and chemical characteristics from that of the bulk substance. These differences have

a significant effect on the substance's top atomic layer. The molecule is continuously surrounded in the middle of the substance in all directions by atoms that make up the material. Because the surface atom is not surrounded by atoms in both directions, it has a bonding potential that makes the surface atom receptive to bulk atoms [5].

1.2.2. Inelastic mean free path (IMFP)

When an Ultraviolet photon or X-rays impact the sample, the photoelectrons with characteristic energies are generated inside the sample. To be measured, these photoelectrons should move to the surface and leave the surface. However, such electrons may collide with atomic electrons and by ionizing atoms to lose their characteristic energies before arriving surface derived from atoms, travel through matter over a certain distance until reaching the surface. It is important to know the distance an electron will go through matter while retaining its kinetic energy. Figure 1.3 demonstrate dependence between IMFP and kinetic energy in XPS. The mean distance between two inelastic collisions is known as the IMFP λ, and it is defined by formula 1.2 [8].

$$I(d) = I_0 e^{-d/\lambda(\mathrm{E})}, \qquad (1.2)$$

where $I(d)$ is the intensity following the primary electron beam passing through the solid to a distance d. Thus the IMFP $\lambda(d)$ defines the distance at which the electron beam intensity decreases e (equal approximately 2.73) times in comparison with the initial value. λ is also called as the attenuation length.

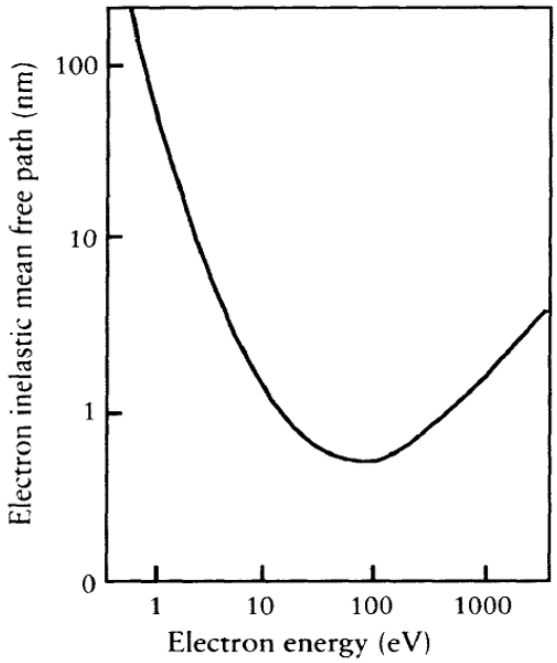

Figure 1.3. Graph of dependence between of IMFP and kinetic energy in XPS [5].

1.2.3 Surface sensitivity of XPS

UPS also exhibits a greater surface sensitivity than XPS (shown in Figure 1.4), because of the low IMFP within the solid, where more than it is assumed that 95 % of the photoemission signal is originating from the layer with a depth of 3 mean free path lengths from the surface [5]. Consequently, UPS also exhibits a greater surface sensitivity than XPS (shown in Figure 1.4), because of the low IMFP within the solid. For XPS, the thickness on the studied layer is assumed to be below, 10 nm. That is the crude average since the IMFP of the electron is determined by the material properties and the kinetic energy of the electrons in solid media over which it passes and electrons of lower kinetic energy having shorter path lengths [6].

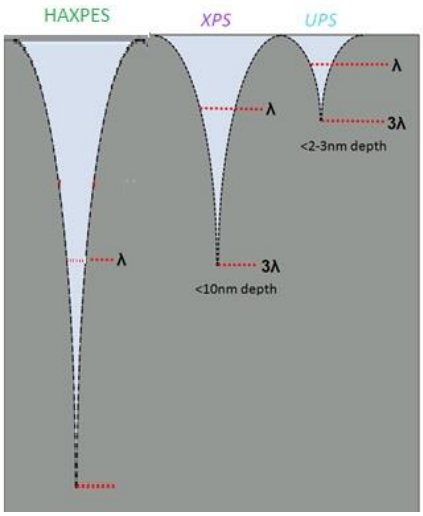

Figure 1.4. Difference in information depth for HAXPES, XPS and UPS [7].

1.2.4 XPS at different angles

The knowledge range for XPS is a few nanometers, based on the kinetic energy of the electrons and the substance being analyzed. XPS measured at different angles is, however, a method that changes the emission angle from which electrons are emitted, making it easier to detect electrons from various depths (Figure 1.5). Angle-resolved XPS provides knowledge on the size and structure of ultra-thin films. Those tests are non-destructive, as opposed to sputter profiling [5].

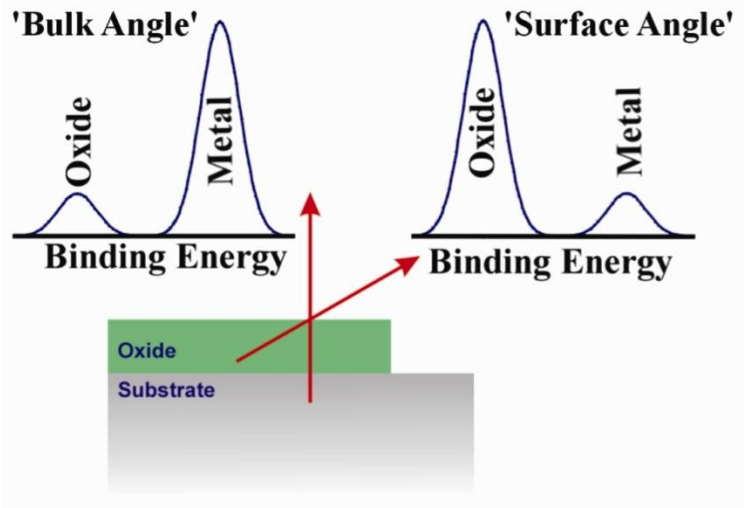

Figure 1.5. Spectra with a higher relative intensity of the oxide peak at the close to grazing emission angle may be seen from an examination of a thin oxide film on a metal at near-normal and non-grazing angles [7].

Key useful aspects of XPS with variable angles:

- Can be extended to films that are too thin to be studied using standard depth profiling techniques.
- Can be extended to films that are irretrievably damaged by sputtering (e.g. polymers).
- Non-destructive technique and can provide details on the chemical environment, unlike sputtering methods.

The following information is given by the Angle-resolved XPS measurements:

- Ordering of layers in an ultra-thin film.
- Thickness of layers
- Distribution of elements and chemical states within the film (depth profile reconstruction) [5].

1.3 Photoelectron spectrum

A photoelectron spectrum is a record of the photoelectron intensity as a function of the photoelectron kinetic energies at fixed photon energy. However, in addition to photoelectron peaks, other features are present in the spectrum. Usually, these bands are related to Auger electrons, but also to shake-up satellites, shake-off satellites and multiplet splitting can arise.

Auger effect is based on simultaneous ejection of an electron when core hole is filled at the same atom. Auger transition is an inner atomic process, and the Auger electron kinetic energy does not depend on photon energy as does the photoelectron kinetic energy.

Shake-up satellites are formed, when the outgoing photoelectron simultaneously interacts with a valence electron and excites it to a higher energy level. This process leads to the decrease of the

energy of the ejected core electron and satellites appear in photoelectron spectra. Shake-up satellites are few electron volts below the core level position. This process can be accompanied by the formation of a shake-off satellite. The shake-off satellite is formed in the way that a valence electron is ejected from the ion.

A multiplet splitting may arise in a compound that has an unpaired electron in the valence band. When a core hole is created through photoionization, there can be coupling between the unpaired electron in the core-shell with an unpaired electron in the outer shell. This can create a number of final states, which arise in the photoelectron spectrum as a multipeak structure [5].

1.4 Chemical shift

XPS is an excellent tool to identify elements in the surface layer since all elements have their core levels at specific energies as compared to each other. Also, XPS is a useful tool to determine the chemical state of surface atoms. For example, electrons in metal have specific Coulombic interaction between the nucleus and electrons. When oxide is formed, metal transfers its electron to oxygen due to its larger electronegativity. This results as a stronger Coulombic interaction between the nucleus and electrons. Therefore, the binding energy of an electron is larger in metal oxide than in a pure metal, and a "chemical shift" between two compounds is observed [9]. Example of the chemical shifts in N1s is shown in Figure 1.6.

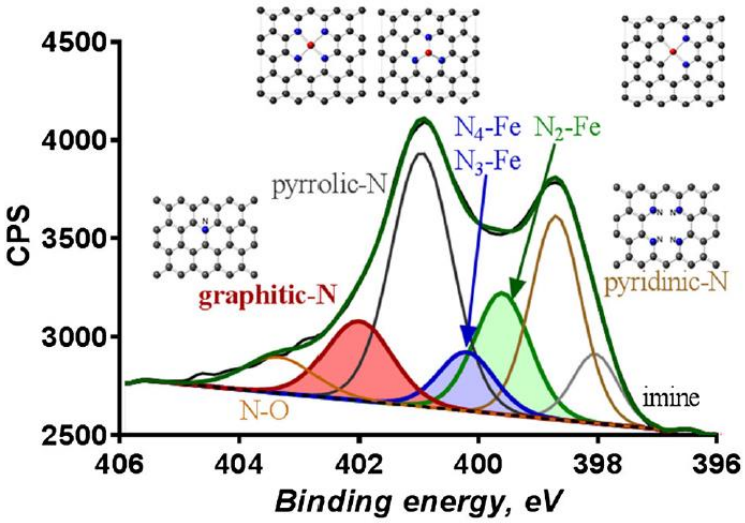

Figure 1.6. High-resolution N1s XPS spectrum [10].

The numerous nitrogen moieties, such as pyridinic-N, pyrrolic-N, graphitic-N, amine/metal-N, imine and others are one of the main subjects for analysis in this study. One of the important concerns is the nitrogen component that contributes to the increased ORR catalytic activity, including pyridinic-N, pyrrolic-N and graphitic-N. N dopants change local electronic properties and surface

chemistry of carbon materials while improving oxygen adsorption and the ORR kinetics substantially. Due to their high abundance in most nitrogen-doped carbon materials, pyridinic-N and graphitic-N have attracted great attention among the nitrogen sites [11].

1.5 Quantification XPS

The intensity I of a photoelectron peak from a homogeneous solid is given by formula 1.3 [5]:

$$I = J\rho\sigma K\lambda, \tag{1.3}$$

where J is the photon flux, ρ is the ion concentration, σ is a cross-section for the output of photoelectron (depending on the element and the energy considered), K is the value covering all the instrumental variables, and λ is the attenuation length.

The referred intensity is usually taken as the integrated region under the peak after linear correction. The above equation can be used for direct quantification (the "first principles approach"), but experimentally defined sensitivity factors F are more widely used. In the typical equation, parameter F contains σ, K, and λ as well as additional photoelectron spectrum components, such as characteristic attribute. When a set of peak areas for the elements found has been measured, I was defined in the mentioned equation. The components σ, K, and λ are integrated into or specifically included in the formula used to measure a series of sensitivity factors suitable for the used spectrometer (formula 1.4). If the X-ray flux remains stable in the experiment, the atomic percentage of the elements can be calculated by dividing the peak area by the sensitivity factor and expressing it as a fraction of the sum of all normalized intensities; the surface composition measurement for this approach assumes that the measured volume of a sample is homogeneous:

$$[A]\ atomic\ \% = \left\{\frac{\frac{I_A}{F_A}}{\Sigma\left(\frac{I_i}{F_i}\right)}\right\} \cdot 100\%, \tag{1.4}$$

This is uncommon, but the above approach provides a valuable way to compare related specimens. XPS can be used to maintain lateral homogeneity and elucidate the hierarchy of overlayers present for a more comprehensive analysis [5, p. 75-76].

2. INSTRUMENTATION

Photoelectron spectrometer contains source (He lamp or X-ray tube), electron energy analyzer, manipulator with sample holder and vacuum chamber (Figure 2.1).

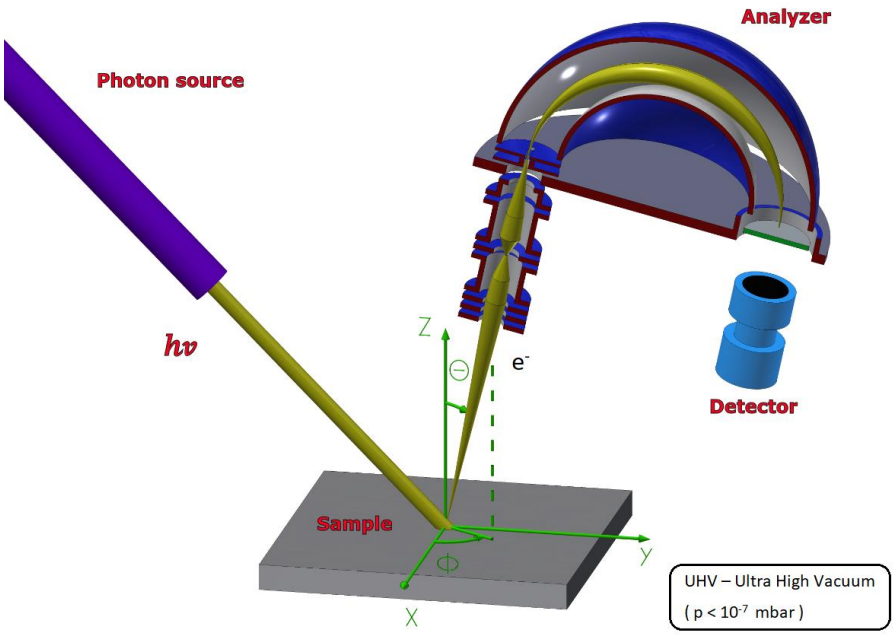

Figure 2.1. A photoelectron spectrometer design. [based on 7]

The detector counts a number of photoelectrons inside a certain kinetic energy interval.

The spectrometer should have ultrahigh vacuum (approximately 10^{-9} mbar) inside the chamber to prevent electrons and photons from being scattered by gas molecules. [5].

The electron lens (Figure 2.2) collects the electrons from the sample and passes them to the entrance of the energy analyzer. The lens has a variety of purposes [12]:

- Physically isolate the sample region from the energy analyzer, allowing better accessibility of the sample.
- Generating a photoelectron image of the sample on the entrance plane of the analyzer, such as a focusing lens.
- Match the initial kinetic energy of the electrons to the output energy of the analyzer.

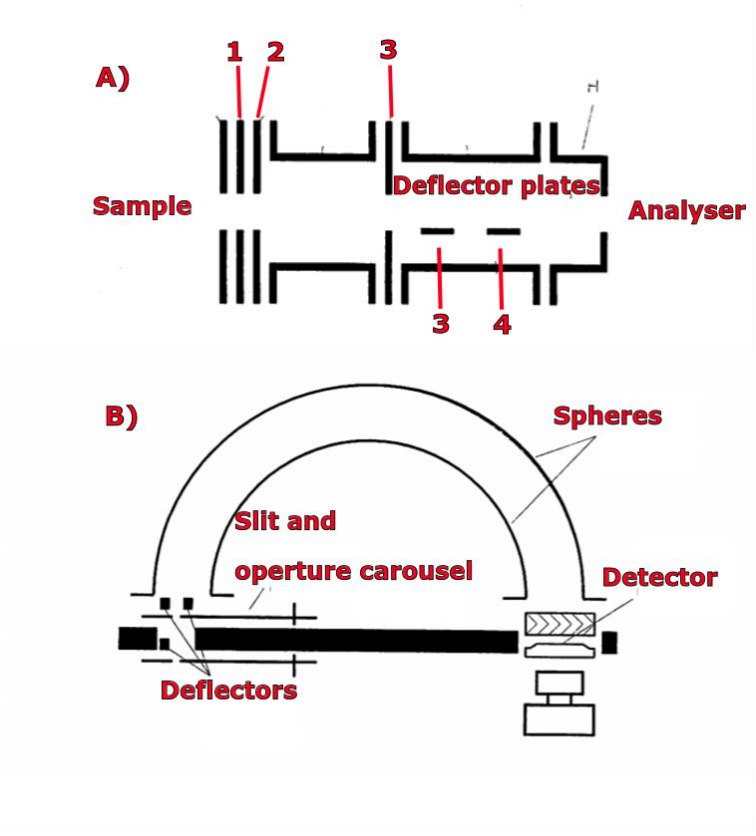

Figure 2.2. A scheme of the electrostatic lens (a), where 1 - ground potential, 2 - element for the elimination of the penetration from lens into the space between the sample and the lens entrance, 3 - detail for optimization of the lens parameter, 4 - connection to the retardation/acceleration voltage and schematic illustration of the hemispherical analyzer (b) [12].

The hemispherical electron energy analyzer (Figure 2.2) is the part of the device that performs the actual energy dispersion. In the radial electrostatic field, the electron trajectories are twisted between two concentric hemispheres with a voltage difference between them. The bending radius will depend on the electron kinetic energies, and an energy dispersion is achieved. The 180° hemisphere analyzer has some advantages compared to other analyzer types, the most prominent of which is the existence image plane with unit magnification perpendicular to the trajectories. This instrument is equipped with an analyzer with a mean radius of 100 mm. The field is terminated by a plate on the center potential of the analyzer, which also serves as the mechanical base for the electrode structure. The analyzer is equipped with a deflection electrode close to the entrance slit [12].

For measurements in the frame of this thesis Thermo XR3E2 Twin Anode X-ray source was used (Figure 2.3). The principle elements of the X-ray Source are supported by the Source Mounting Flange. The anode, which sits on an annealed copper gasket, is placed through the Source Mounting Flange to project through the Filament Inner Shield. The position of the anode within the Filament Inner Shield is centralized by three ceramic bushes. The Filament mounted concentrically with the Filament Inner Shield is enclosed by the Filament Outer Shield in which is fitted a very thin aluminum

foil window. The electrical connections to the Double Filament are made through three Filament Electrodes mounted on the three single-way feedthrough connectors in the Source Mounting Flange. The high voltage connection to the anode is made through the pipes, which supply cooling water to the anode region of the source, and the connections are made using "Quick-Fit" connectors providing a safe and rapid method of removing cables and water lines before go out [13].

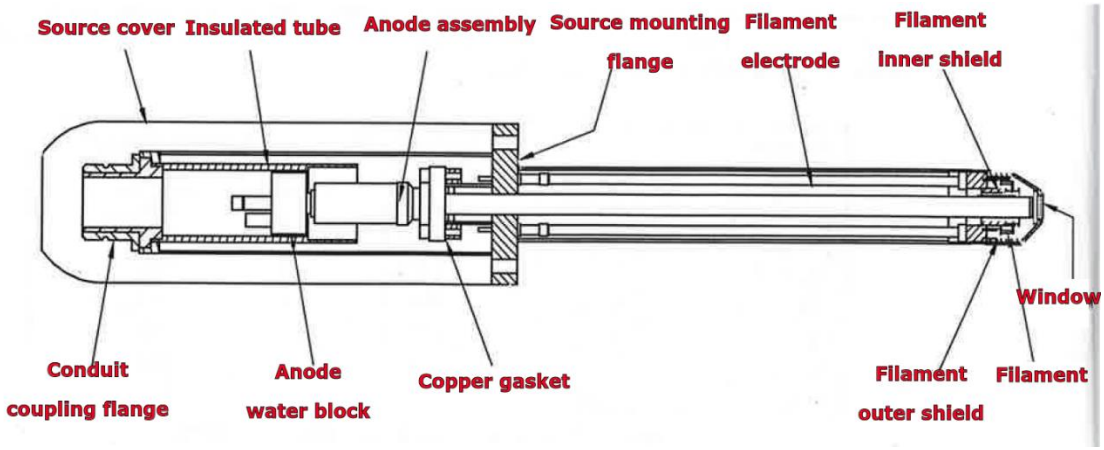

Figure 2.3. Scheme of the XR3E2 X-ray source [13].

3. EXPERIMENTAL

3.1 Materials

Renewable power generated by hydrogen fuel cells is a potential alternative solution to the issue of fossil fuel consumption. Porous carbon is a basic material in polymer electrolyte membrane (PEM) fuel cells [2].

In this work were investigated two sets of electrocatalysts. Kaido Tammeveski's research group synthesized all investigated samples. My part was measurements of photoelectron spectra of electrocatalysts and interpretations of these spectra.

Samples A1-Fe, A2-Co, A3-Fe and A4-Co were synthesized with 5-methylresorcinol (5MR, purity 99.9%, VKG Oil AS, Estonia), dicyandiamide (DCDA, Sigma-Aldrich), $Co(NO_3)_2$ (98%, Sigma-Aldrich) and/or $FeCl_3$ (97% Sigma-Aldrich). The ratio of precursors was varied at the first optimization stage. The 5MR-to-DCDA mass ratio of 1:10 was used in most samples, and the precursor compounds were dissolved in a mixture of 2-propanol and deionized water (Milli-Q, Millipore Inc.) with a volume ratio of 1:4. Then $Co(NO_3)_2$ or $FeCl_3$ were added at the metal-to-5MR mass ratio of 1:20. The solution has been dried for 48 h at 35 °C, and the dry powder was pyrolyzed at 800 °C in the N_2 flow for 2 h. The carbon-based catalysts were obtained after cooling down to room temperature. In a mixture of 0.5 M HNO_3 and 0.5 M H_2SO_4, the materials A1-Fe and A2-Co

were acid-treated at 50 °C for 8 h, washed with Milli-Q water, dried and pyrolyzed at 800 °C for 2 h to obtain the final catalysts.

Samples SiCDC HiB BM1, SiCDC HiB BM3 and SiCDC HiB BM4 based on CDC and were milled under different conditions:

- SiCDC HiB BM1 was prepared using the milling procedure as follows: 400 rpm, 4x30 (5 min breaks), ≈ 100 mg CDC, ZrO_2 balls (diameter 5 mm), so-called dry-ball-milling with larger ZrO_2 balls.
- SiCDC HiB BM3 was prepared using the milling procedure as follows: 400 rpm, 4x30 (5 min breaks), ≈ 200 mg CDC, ZrO_2 balls (diameter 0.5 mm, mass 20 mg), ca 2.5 mL Milli-Q, so-called wet-ball-milling with smaller ZrO_2 ball.
- SiCDC HiB BM4 was prepared using the milling procedure as follows: 400 rpm, 4x30 (5 min breaks), ≈ 1200 mg CDC, ca 20 mg PVP, ZrO_2 balls (diameter 0.5 mm, mass 20 mg), ca 3 mL Milli-Q water, so-called wet-ball-milling with small ZrO_2 balls in the presence of polyvinylpyrrolidone.

3.2 Sample preparation

For XPS experiment, the sample should be with optimal size and geometry for the sample holder (approximately 10x10 mm). To keep samples clean during sample preparation, it is necessary to use gloves and appropriate precleaned tools.

The mounted sample is introduced into a load-lock chamber. After pumping the load-lock chamber, the sample is transferred to the analysis chamber under vacuum (pressure approximately 10^{-9} mbar). The sample is rotated 180° after the transfer into an analysis chamber and positioned against an electron energy analyzer. The angle between the sample normal to the incident X-ray beam is 45°, and the angle from the analyzer to the incident X-ray beam is 45°.

3.3 Equipment

Experiments were performed to characterize samples for elemental compositions by XPS surface science setup (Figure 3.1) with analyzer SCIENTA SES-100 and unmonochromated XR3E2 twin anode X-ray source. Mg Kα X-rays (energy 1253.6 eV) at 300 W power and electron take-off angle 90° were used. During obtaining the XPS spectra, the pressure in the analysis chamber was under 10^{-9} mbar. For collecting survey spectra and high-resolution spectra the step sizes of 1 eV and 0.1 eV, respectively, were used.

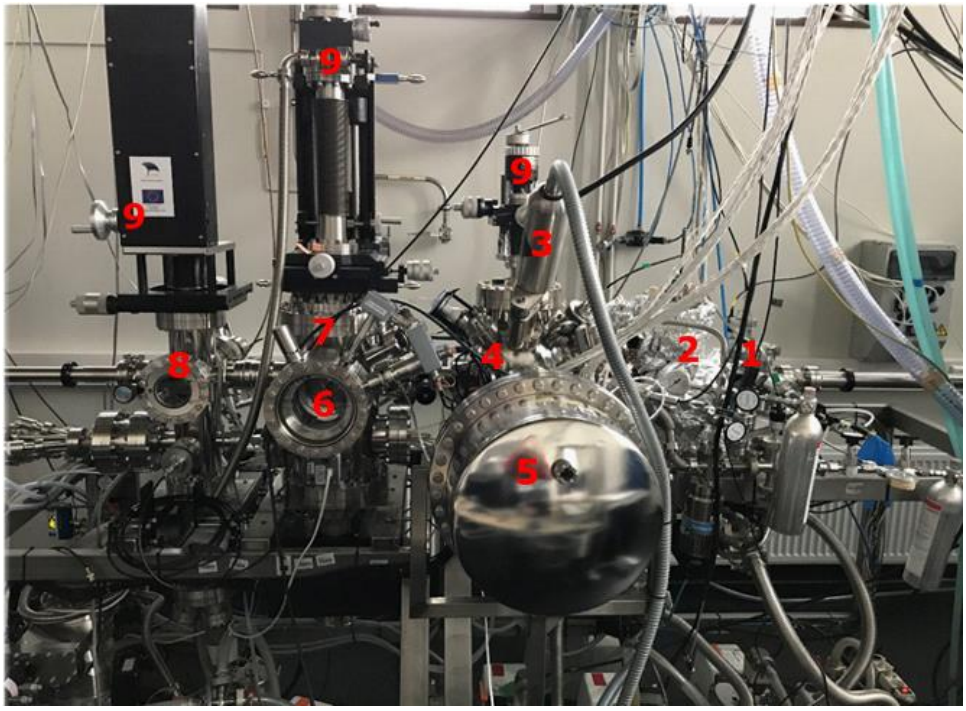

Figure 3.1. Surface-science setup, which contains 1 – load-lock chamber, 2 – preparation chamber, 3 – X-ray gun, 4 – XPS analysis chamber, 5 –SCIENTA SES-100 electron energy analyzer, 6 – LEED optics, 7 – LEED analysis chamber, 8 – load-lock/preparation chamber, 9 – manipulator.

3.4 XPS data treatment

Data analysis and quantification were performed using CasaXPS software. Sensitivity factors provided by the manufacturer were utilized. In the analysis of the XPS spectra we used offset Shirley type background (see section 3.4.1-3.4.3). Photoelectron lines were fitted with a 70% Gaussian/30% Lorentzian line shape (see section 3.4.4) and Gaussian/Lorentzian product modified by an asymmetric form.

3.4.1 Linear background

For materials with large band-gaps linear background can be used $L(E)$:

$$L(E) = I_1 \frac{(E_2 - E)}{(E_2 - E_1)} + I_2 \frac{(E - E_1)}{(E_2 - E_1)}, \quad (3.1)$$

where E_1 and E_2 are two different energies, and I_1 and I_2 are corresponding intensities [14].

3.4.2 Shirley background

The Shirley algorithm [15] is an attempt to use spectrum information to create a background that is sensitive to data adjustment. The main feature of the Shirley algorithm is the iterative background calculation using the designated areas A_1 and A_2 in order to compute the background $S(E)$ of energy E:

$$S(E) = I_2 + k\frac{A_2(E)}{(A_1(E)-A_2(E))}, \quad (3.2)$$

where k determines the background phase and typically is the same $(I_1 - I_2)$. For each point in background E, the built-in areas $A_1(E)$ and $A_2(E)$ must be determined initially using a $S(E)$ approximation and then optimized using the first estimated history computed as a reference to boosting the values computed for $A_1(E)$ and $A_2(E)$ [14].

3.4.3 Offset Shirley background

Often the blend of linear and Shirley backgrounds is used, called as Offset Shirley (OS) background. It can be written as

$$OS(E:\ \lambda, \delta) = S(E - \ \delta)(1 - \lambda) + L(E)\lambda, \quad (3.3)$$

the parameters λ and δ a linear variation of the background of the Shirley with the background λ=0 with the linear background λ=1, where the Shirley curve is offset by the energy δ eV [14].

3.4.4 Line shapes

Line shape in XPS arises from a combination of the process involved in the event of ionization and deviations broadenings arising from the measurement system. The idealization of these factors is the interpretation of a measured line as a combination of Gaussian (G), and Lorentzian (L) functions. The Gaussian represents the measuring mechanism in general (instrumental function, X-ray line shape, Doppler and thermal broadening) [14]:

$$G(x: E, F, m) = \exp\left[-4\ln 2(1 - \frac{m}{100})\left(\frac{x-E}{F}\right)^2\right], \quad (3.4)$$

Lorentzian models broadening due to lifetime:

$$L(x: E, F, m) = \frac{1}{1+4\frac{m}{100}(\frac{x-E}{F})^2}\ , \quad (3.5)$$

CasaXPS program uses the combination of Gaussian and Lorentzian (GL):

$$GL(x: E, F, m) = \frac{\exp\left[-4\ln 2(1-\frac{m}{100})(\frac{x-E}{F})^2\right]}{1+4\frac{m}{100}(\frac{x-E}{F})^2}, \quad (3.6)$$

The explanation for the calculation of peak intensity is that all functions are finite when combined from minus infinity to plus infinity. In addition, the strength determined by fitting these functions to the data is very localized at the peak for all regular usage of the Gaussian-Lorentzian line shapes. This compares with virtually all asymmetrical line shape, in which the incorporation of asymmetry into the line shape increases the energy spectrum of the line shape and affects the shape's capacity to quantify pressure without adjustment [14].

3.5 Limit of detection (LOD)

Pulsed intensities measured over a time interval are supposed to follow Poisson statistics and, thus if electron energy interval and time intervals counts are recorded, the standard deviation for a sequence of identical measurements in theory is $\sqrt{I}$, intensity.

In the case of low peak intensity and the background area are roughly the same and thus a standard deviation in the measured intensities for low peaks, for a background intensity (B), can be approximated by $\sqrt{B}$.

Since a spectrum can be measured with a variety of energy steps and times instead of the intensity by acquisition bin, the signal intensity is characterized as the intensity falling within a given quantifying area over a defined background.

For an energy interval and acquisition time corresponding to the quantification region with the background type limit of detection (LOD) specified one standard deviation is given by $\sqrt{BN}$, where N is the number of data channels within region limits. The corresponding intensity to be compared with this standard deviation is the sum of the positive background-subtracted counts falling within the LOD_{area} limits.

The test for a peak is the form according to equation 3.7, assuming the behavior of Poisson:

$$if\ (LOD_{area} > factor \cdot \sqrt{BN})\ then\ \text{“}peak\ detected\text{”}, \qquad (3.7)$$

For a 99% confidence level interval and Poisson statistics $factor = 3.0$ [14].

4. RESULTS AND DISCUSSIONS

4.1 General composition of samples

With XPS it became possible to carry out non-destructive chemical analysis of electrocatalysts. XPS survey scans spectra (Figure 4.1 and Figure 4.2) of samples under investigation allow to understand the approximate composition of electrocatalysts. The positions of the peaks are in agreement with comprehensive reference tables (see Appendix 1). The atomic concentration of all series of electrocatalysts, obtained from further analysis using detailed core-level spectra (sections 4.2-4.7) are shown in Tables 4.1 and 4.2.

The XPS survey spectra for A1-A4 samples reveal six distinct photoelectron lines attributed to the binding energies of C1s (≈284.8 eV), N1s (≈397 eV), O1s (≈531 eV), Fe2p (≈709.6 eV) and Co2p (≈778 eV) respectively.

Overview spectra show also a low content of copper (approximately 933 eV), because of the signal of the sample holder, and it is not connected with the catalyst material itself.

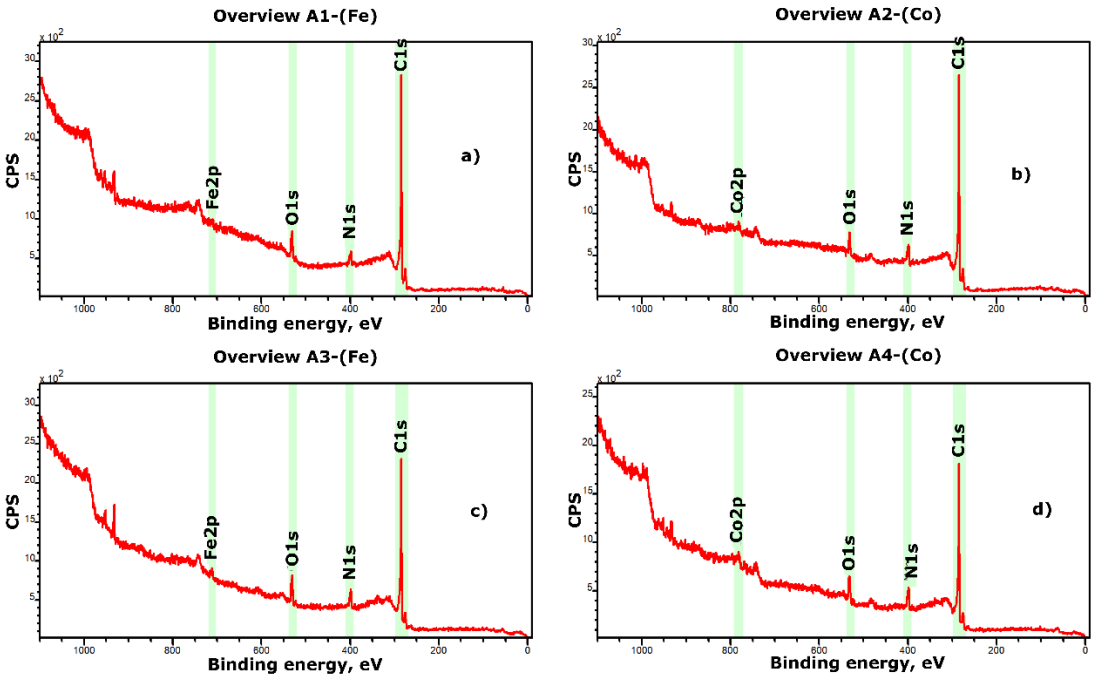

Figure 4.1. XPS survey spectra for A1 (a), A2 (b), A3 (c) and A4 (d) samples, respectively.

Table 4.1. Atomic concentration of A1-A4 samples by elements.

Atomic concentration of A1-A4 samples, %				
Sample	**C1s**	**O1s**	**N1s**	**Metal (Fe or Co)**
A1- (Fe)	88.0	5.9	5.8	0.3
A2 - (Co)	86.7	4.4	8.2	0.7
A3- (Fe)	83.3	7.3	8.9	0.5
A4 - (Co)	82.7	6.3	9.9	1.1

In the XPS survey spectra for SiCDCHibBM1- SiCDCHibBM4 samples appear five distinct peaks attributed to the binding energies of C1s (≈284.8 eV), N1s (≈397 eV), O1s (≈531 eV), Si2p (≈103.5 eV) and Zr3d (≈185 eV), respectively.

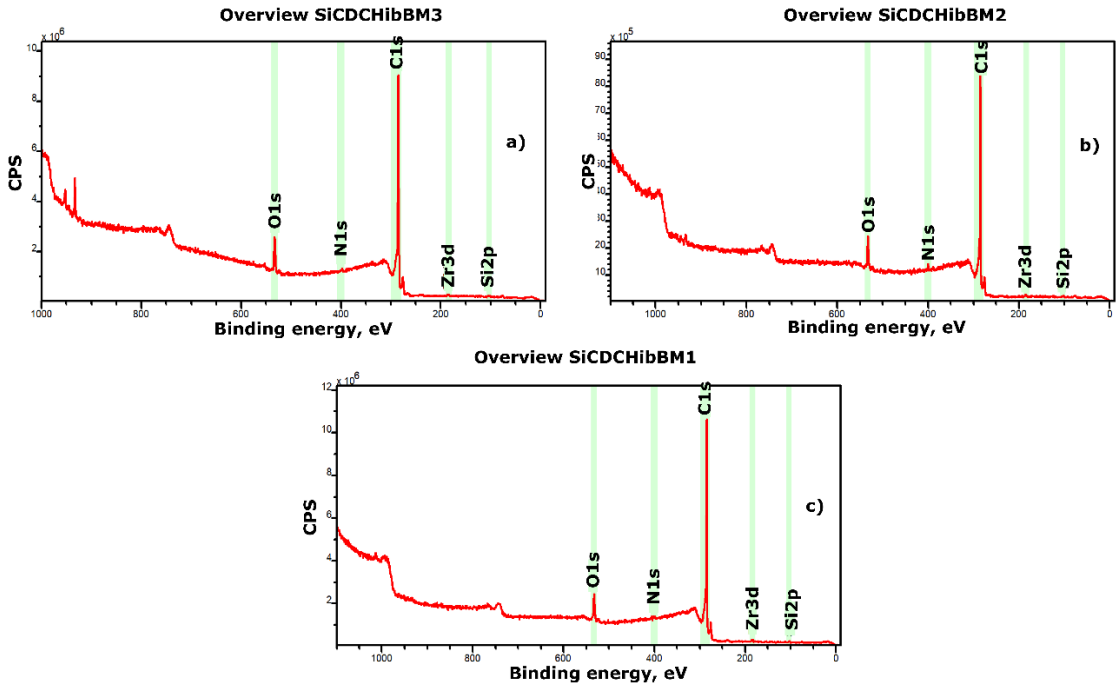

Figure 4.2. XPS survey spectra for SiCDCHibBM3 (a), SiCDCHibBM4 (b) and SiCDCHibBM1 (c) samples, respectively.

Table 4.2. Atomic concentration of SiCDCHibBM1- SiCDCHibBM4 samples by elements.

Atomic concentration of CDC-based samples, %					
Sample	**C1s**	**O1s**	**N1s**	**Si2p**	**Zr3d**
SiCDCHibBM1	83.7	15.0	0.6	0.5	0.2
SiCDCHibBM3	84.3	15.0	0.1	0.5	0.1
SiCDCHibBM4	83.2	15.6	0.6	0.5	0.1

4.2 Measurements of C1s

Carbon is the most abundant component in both sets of electrocatalyst materials (Figure 4.1 and Figure 4.2). The following measurements and analyses allow to show different functional groups on the surface.

C1s detailed core-level spectra (Figure 4.3) for A1, A2, A3 and A4 samples show that C1speak can be decomposed to the sp^2 C (with relative content more than 40%) and other components such as *C-O-C*, *C=O*, *C-O=C*, π- π*, and *carbide*. Note that for sp^2 C asymmetric line shape (typical to conductive states) was used.

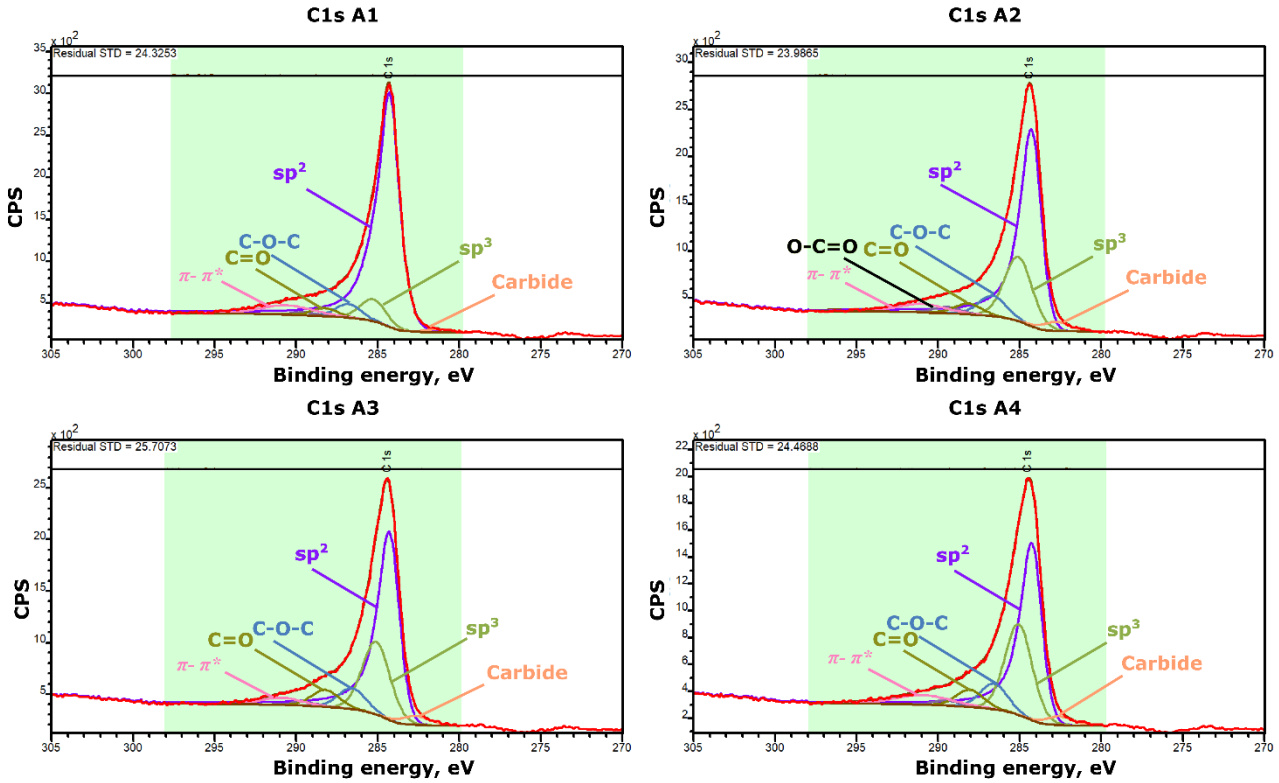

Figure 4.3. XPS detailed core-level spectra in the C1s region for A1 (a), A2 (b), A3 (c) and A4 (d) samples, respectively.

Table 4.3 shows the content of the different C1s states obtained from C1s core-level spectra.

Table 4.3. Concentration of the various C1s states from A1, A2, A3 and A4 samples.

Name	Position, eV	Relative concentration of C1s, %	Atomic concentration of sample, %
A1-(Fe)			
sp^2	284.3	73.2	64.5
sp^3	285.3	8.5	7.5
C-O-C, C-OH	286.8	5.3	4.7
O-C=O	289.5	1.2	1.1
C=O	288.2	3.1	2.8
π- π^*	290.6	7.5	6.6
carbide	281.3	1.1	1.0
A2-(Co)			
sp^2	284.3	52.3	45.3
sp^3	285.1	24.3	21.1
C-O-C, C-OH	286.7	7.8	6.8
O-C=O	289.5	2.5	2.2
C=O	288.2	4.1	3.6
π- π^*	291.0	5.5	4.8
carbide	282.8	3.5	3.0
A3-(Fe)			
sp^2	284.3	50.1	41.8
sp^3	285.1	27.0	22.5
C-O-C. C-OH	286.6	7.8	6.5
O-C=O	289.5	1.4	1.2
C=O	288.2	6.4	5.3
π- π^*	290.9	4.0	3.3
carbide	282.7	3.3	2.8
A4-(Co)			
sp^2	284.3	43.5	35.9
sp^3	285.1	30.5	25.2
C-O-C. C-OH	286.6	8.7	7.2
O-C=O	289.5	1.8	1.5
C=O	288.1	5.9	4.9
π- π^*	290.9	6.7	5.5
carbide	282.6	3.0	2.5

In XPS detailed core-level spectra (Figure 4.4) of C1s for SiCDCHibBM1, SiCDCHibBM3 and SiCDCHibBM4 samples the sp^2 C (with relative content above 40%) and other components such as sp^3, *C-O-C*, *C = O*, *C-O = C*, π- π* and *carbide* components similarly distributed in the spectrum.

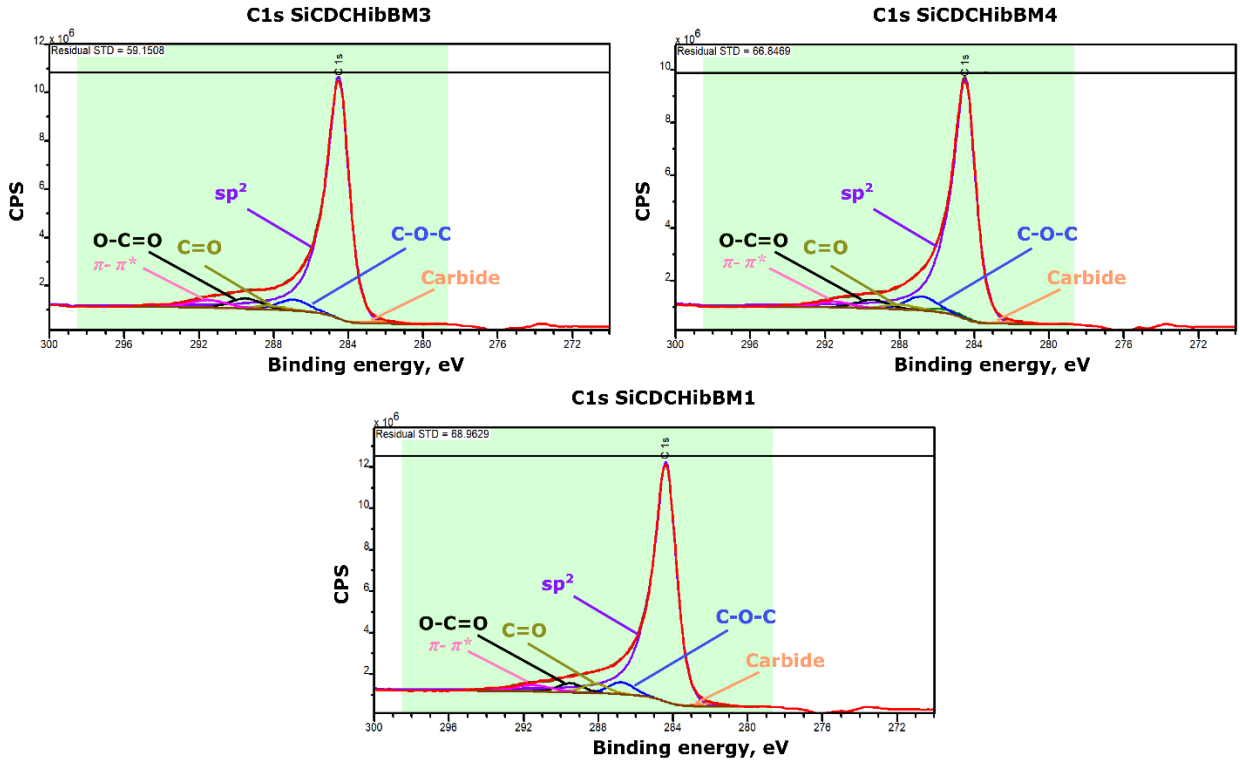

Figure 4.4. XPS detailed core-level spectra in the C1s region for SiCDCHibBM3 (a), SiCDCHibBM4 (b) and SiCDCHibBM1 (c) samples, respectively.

Table 4.4 demonstrates the content of the different C1s states obtained from C1s core-level spectra.

Table 4.4. Concentration of the various C1s states from SiCDCHibBM1, SiCDCHibBM3, SiCDCHibBM4 samples.

Name	Position, eV	Relative concentration of C1s, %	Atomic concentration of sample, %
SiCDCHibBM1			
sp^2	284.4	82.0	68.7
sp^3	285.4	0	0
C-O-C. C-OH	286.8	5.0	4.2
O-C=O	289.5	3.8	3.2
C=O	288.2	3.9	3.3
π- π*	291.5	3.9	3.3
carbide	281.9	1.3	1.1
SiCDCHibBM3			
sp^2	284.5	81.3	68.5
sp^3	285.5	0	0
C-O-C. C-OH	286.9	5.5	4.7
O-C=O	289.5	5.3	4.5
C=O	288.2	1.9	1.6
π- π*	291.5	4.7	4.0
carbide	282.0	1.2	1.0
SiCDCHibBM4			
sp^2	284.5	80.4	66.9
sp^3	285.5	1.8	1.5
C-O-C. C-OH	286.8	6.8	5.7
O-C=O	289.5	4.3	3.6
C=O	288.0	2.3	1.9
π- π*	291.5	3.1	2.6
carbide	281.8	1.2	1.0

4.3 Measurements of N1s

Nitrogen species such as graphitic-N and pyridinic-N play significant role in the ORR. The deconvolution of the electrocatalysts' N1 XPS detailed core-level spectra shows seven different peaks.

In N1s detailed core-level spectra (Figure 4.5) for A1, A2, A3 and A4 samples the peak attributed to *pyridinic*-N and *pyrrolic*-N significantly dominates in spectra, and other components such as *amines/metal-Nx, imine, graphitic-N, NO* and *bulk N-H* have lower intensities in the spectra.

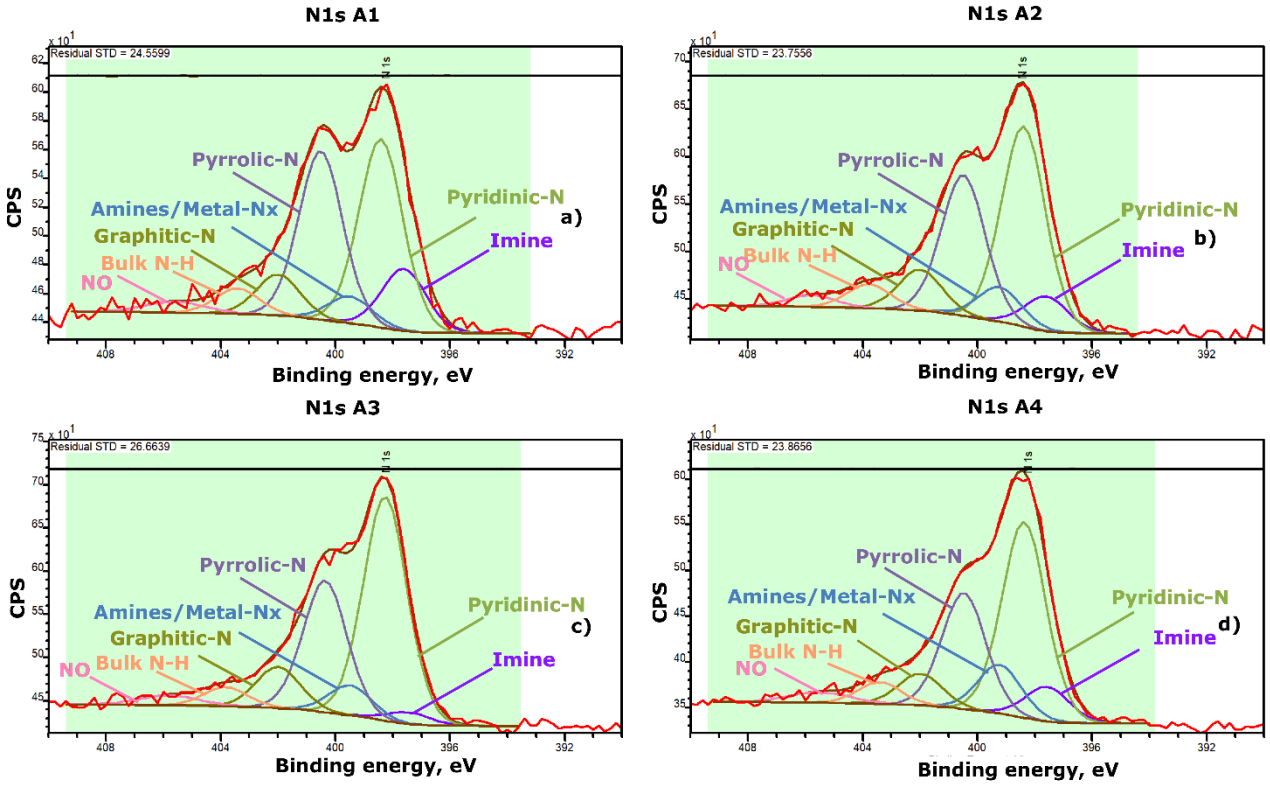

Figure 4.5. XPS detailed core-level spectra in the N1s region for A1 (a), A2 (b), A3 (c) and A4 (d) samples, respectively.

Table 4.5 presents the content of the different N1s states obtained from N1s core-level spectra.

Table 4.5. Concentration of the various N1s states from A1, A2, A3 and A4 samples.

Name	Position, eV	Relative concentration of N1s, %	Atomic concentration of sample, %
A1-(Fe)			
Imine	397.6	11.9	0.7
Pyridinic-N	398.4	35.6	2.1
Amines/Metal-Nx	399.5	5.2	0.3
Pyrrolic	400.5	32.0	1.9
Graphitic	402.0	7.7	0.5
NO	405.6	2.9	0.2
bulk N-H	403.4	4.8	0.3
A2-(Co)			
Imine	397.6	7.1	0.6
Pyridinic-N	398.4	41.0	3.4
Amines/Metal-Nx	399.2	7.0	0.6
Pyrrolic	400.5	28.8	2.4
Graphitic	402.0	8.4	0.7
NO	405.8	2.7	0.2
bulk N-H	403.8	5.0	0.4
A3-(Fe)			
Imine	397.5	2.5	0.2
Pyridinic-N	398.3	47.5	4.2
Amines/Metal-Nx	399.5	6.3	0.6
Pyrrolic	400.4	27.9	2.5
Graphitic	402.0	8.7	0.8
NO	405,8	3.0	0.3
bulk N-H	403,8	4.1	0.4
A4-(Co)			
Imine	397,6	7.5	0.7
Pyridinic-N	398,4	42.2	4.2
Amines/Metal-Nx	399,2	10.5	1.0
Pyrrolic	400,5	25.0	2.5
Graphitic	402,0	6.9	0.7
NO	405,5	3.2	0.3
bulk N-H	403,4	4.7	0.5

In N1s detailed core-level XPS spectra (Figure 4.6) for SiCDCHibBM4 and SiCDCHibBM1 samples, the peaks attributed to moieties such as *pyrrolic-N graphitic-N* and *amines/metal-Nx* are strongest and other components such as *NO* and *bulk N-H,* have rather low intensities. *Imine* and *water* connected peaks were not observed in SiCDCHibBM4 and SiCDCHibBM1 samples. Presence

of *pyridinic-N* was not found in SiCDCHibBM4; nonetheless, the high intensity of this peak was observed in SiCDCHibBM1.

Results of the XPS measurements for SiCDCHibBM3 shows no significant presence of N1s.

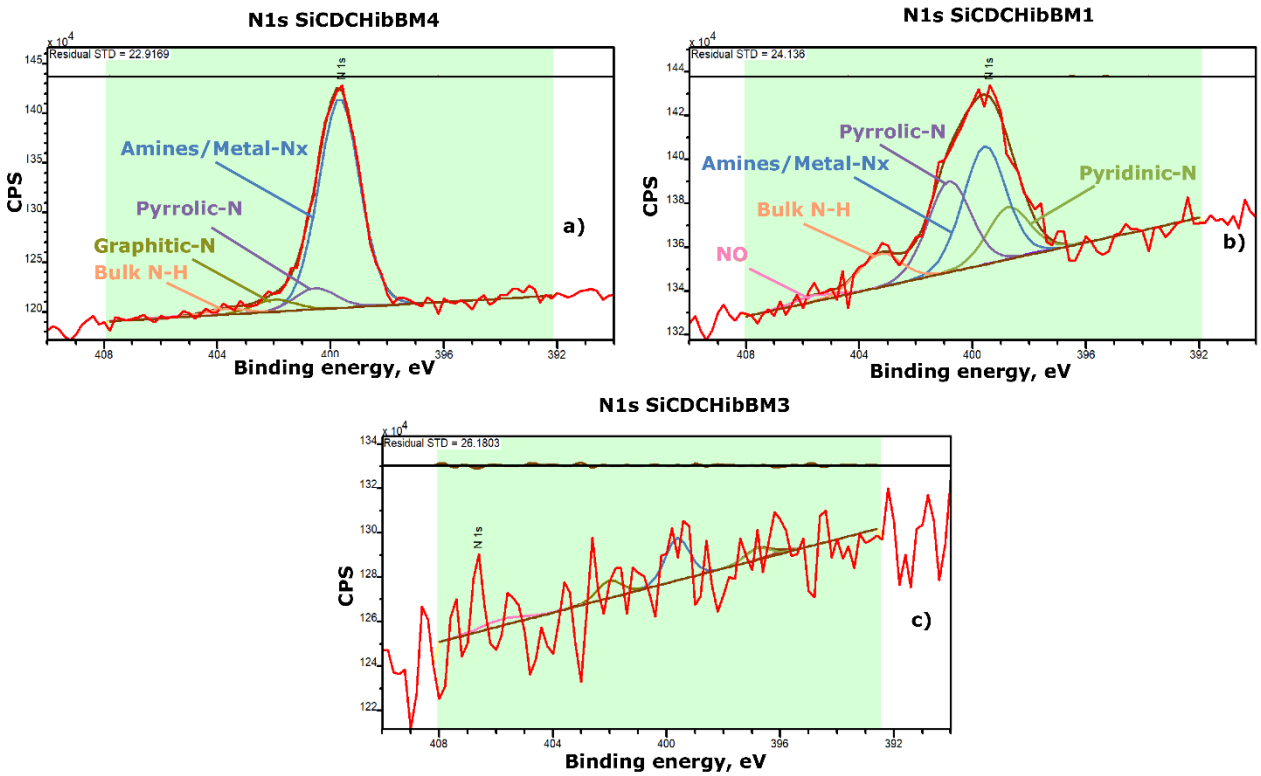

Figure 4.6. XPS detailed core-level spectra in the N1s for SiCDCHibBM4 (a), SiCDCHibBM1 (b) and SiCDCHibBM3 (c) samples, respectively.

Table 4.6 shows the content of the different N1s states obtained from N1s core-level spectra of CDC-based samples.

Table 4.6. Concentration of the various N1s states from SiCDCHibBM1, SiCDCHibBM3, SiCDCHibBM4 samples.

Name	Position, eV	Relative concentration of N1s, %	Atomic concentration of sample, %
SiCDCHibBM1			
Imine	397.9	0	0
Pyridinic-N	398.7	26.2	0.2
Amines/Metal-Nx	399.6	8.2	0.1
Pyrrolic	400.8	45.9	0.3
Graphitic	402.1	0	0
NO	405.6	3.3	0
bulk N-H	403.3	16.4	0.1
SiCDCHibBM3			
Imine	396.0	0	0
Pyridinic-N	396.8	0	0
Amines/Metal-Nx	399.6	0	0
Pyrrolic	398.9	0	0
Graphitic	402.0	0	0
NO	405.8	0	0
bulk N-H	403.0	0	0
SiCDCHibBM4			
Imine	397.7	0	0
Pyridinic-N	398.5	0	0
Amines/Metal-Nx	399.7	43.1	0.3
Pyrrolic	400.6	29.3	0.2
Graphitic	402.0	17.2	0.1
NO	405.8	1.7	0
bulk N-H	403.7	8.6	0.1

4.4 Measurements of O1s

In XPS spectrum O1s is one of the essential components of both sets of electrocatalysts. Measurements and evaluation will reveal various oxygen-containing functional groups on the surface.

In O1s detailed core-level XPS spectra (Figure 4.7) for A1, A2, A3, and A4, was measured showing atomic concentrations of *metal oxide*, *O=C-OH carboxyl*, *C=O carbonyl* and *C-O*. The XPS wide-scan spectrum does not show any observed *quinones* across all catalysts. The *C-OH* compound was not observed in the A3, and A4 samples, however, low intensity revealed in the A1 and A2 samples. *Water* connected peaks have similar low intensities in all samples except A4.

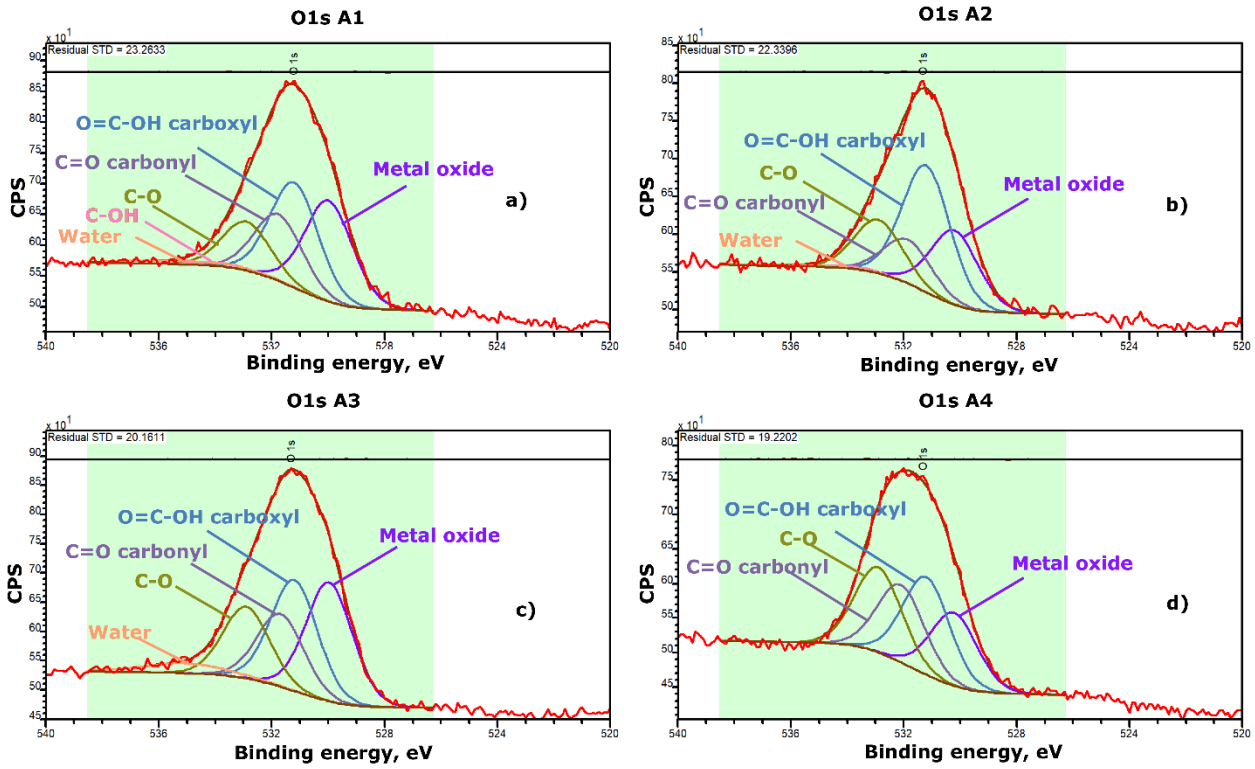

Figure 4.7. XPS detailed core-level spectra in the O1s region for A1 (a), A2 (b), A3 (c) and A4 (d) samples, respectively.

Data obtained from the deconvolution of O1s XPS spectra are given in Table 4.7.

Table 4.7. Concentration of the various O1s states from A1, A2, A3 and A4 samples.

Name	Position, eV	Relative concentration of O1s, %	Atomic concentration of sample, %
A1-(Fe)			
Metal oxide	530.0	30.3	1.8
Quinones	530.2	0	0
O=C-OH carboxyl	531.2	31.5	1.8
C=O carbonyl	531.8	20.0	1.2
C-O	532.9	14.7	0.9
C-OH	533.7	1.0	0.1
Water. Chemisorbed O	535.0	2.6	0.2
A2-(Co)			
Metal oxide	530.2	24.6	1.1
Quinones	530.2	0	0
O=C-OH carboxyl	531.2	41.6	1.8
C=O carbonyl	531.9	14.5	0.6
C-O	532.9	17.7	0.8
C-OH	533.7	0.7	0.0
Water. Chemisorbed O	536.0	0.9	0.0
A3-(Fe)			
Metal oxide	530.0	30.3	2.2
Quinones	530.2	0	0
O=C-OH carboxyl	531.2	28.2	2.1
C=O carbonyl	531.7	18.6	1.4
C-O	532.9	18.3	1.3
C-OH	533.6	0	0
Water. Chemisorbed O	535.1	4.5	0.3
A4-(Co)			
Metal oxide	530.2	22.0	1.4
Quinones	530.2	0	0
O=C-OH carboxyl	531.2	29.3	1.8
C=O carbonyl	532.1	23.2	1.5
C-O	532.9	25.5	1.6
C-OH	533.7	0	0
Water. Chemisorbed O	536.0	0	0

For SiCDCHibBM3, SiCDCHibBM4, and SiCDCHibBM1 samples, detailed core-level XPS spectra of O1 (Figure 4.8) show that peaks attributable to *O=C-OH carboxyl*, *C=O carbonyl*, *C-O* and *water* of a significant atomic concentration have been identified. The wide-scan XPS spectra

show no detected C-OH and quinones among all electrocatalysts. Metal oxide has been observed with low intensity in the entire set of CDC-based catalysts.

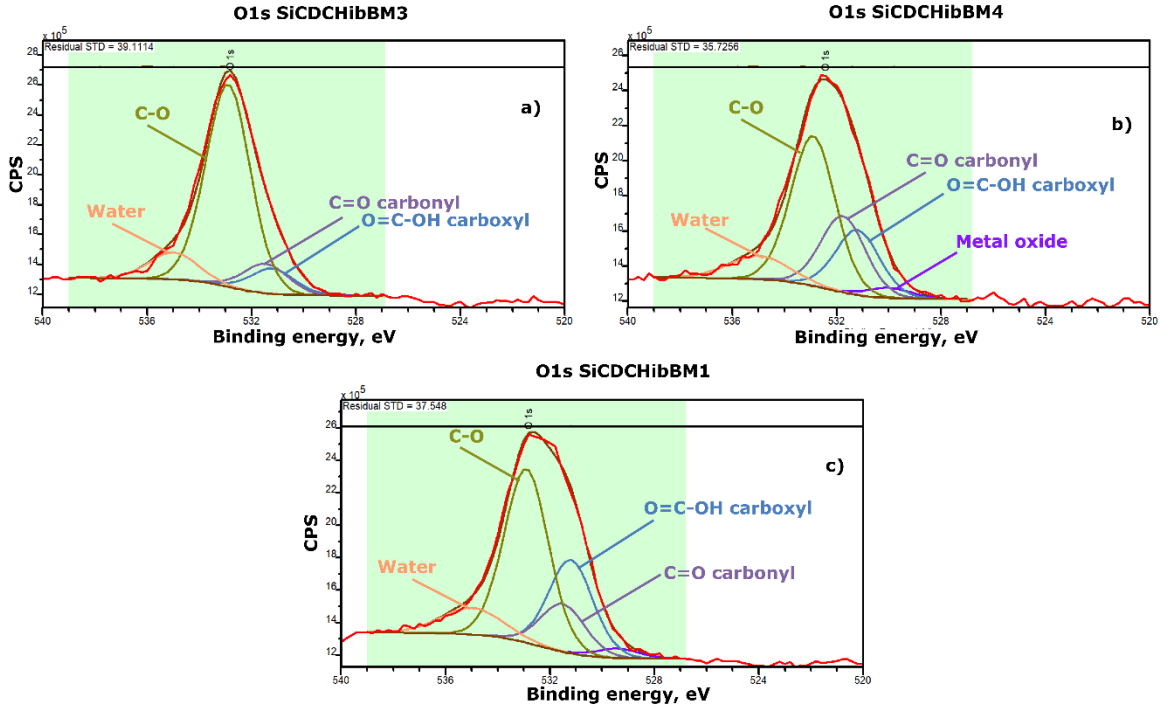

Figure 4.8. XPS detailed core-level spectra in the O1s region for SiCDCHibBM3 (a), SiCDCHibBM4 (b) and SiCDCHibBM1 (c) samples, respectively.

Table 4.8 lists the content of oxygen-containing obtained from O1s core-level spectra states in CDC-based electrocatalyst.

Table 4.8. Concentration of the various O1s states from SiCDCHibBM1, SiCDCHibBM3, SiCDCHibBM4 samples.

Name	Position, eV	Relative concentration of O1s, %	Atomic concentration of sample, %
SiCDCHibBM3			
Metal oxide	529.6	0.2	0
Quinones	530.2	0	0
O=C-OH carboxyl	531.2	8.7	1.3
C=O carbonyl	531.5	10.2	1.5
C-O	532.9	70.5	10.6
C-OH	533.7	0	0
Water. Chemisorbed O	535.0	10.4	1.6
SiCDCHibBM4			
Metal oxide	530.0	3.1	0.5
Quinones	530.2	0	0
O=C-OH carboxyl	531.2	19.4	3.0
C=O carbonyl	531.8	22.9	3.6
C-O	532.9	45.0	7.0
C-OH	533.7	0	0
Water. Chemisorbed O	535.0	9.6	1.5
SiCDCHibBM1			
Metal oxide	529.4	2.5	0.4
Quinones	530.2	0	0
O=C-OH carboxyl	531.2	25.8	3.9
C=O carbonyl	531.5	13.2	2.0
C-O	532.9	48.1	7.2
C-OH	533.7	0	0
Water. Chemisorbed O	535.0	10.4	1.6

4.5 Measurements of Co2p and Fe2p

The XPS core-level spectra in the Co2p (Figure 4.9) and Fe2p (Figure 4.10) regions contain multiple peaks that are associated with oxidized metal states, which may be bulk oxides, but also metal coordinated to nitrogen. It is, however, impossible to classify these components specifically, because there are different metal species with overlapping states. Components in fitting were selected to cover the area of photoelectron lines. Due to overlapping with KLL transition (approximately 740 eV) of oxygen, only the area of $Fe2p_{2/3}$ was analyzed.

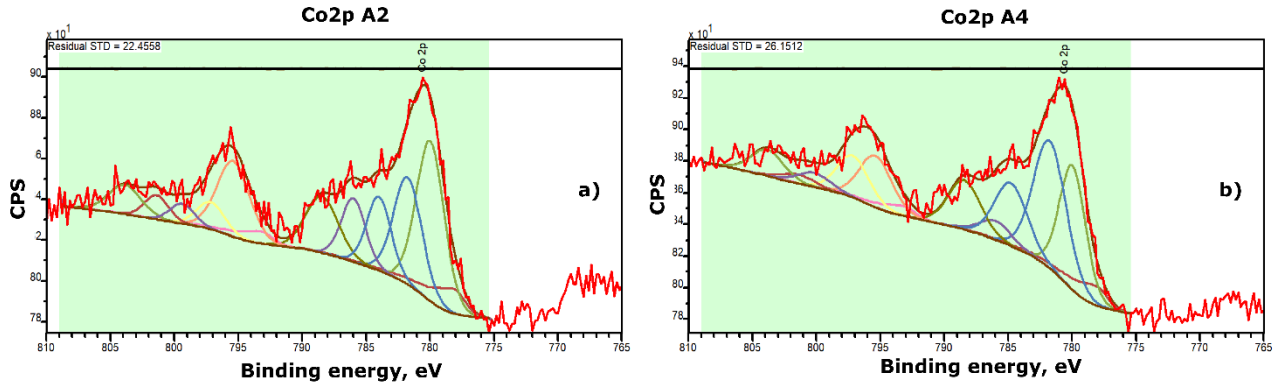

Figure 4.9. XPS detailed core-level spectra in the Co2p region for A2 (a) and A4 (b) samples, respectively.

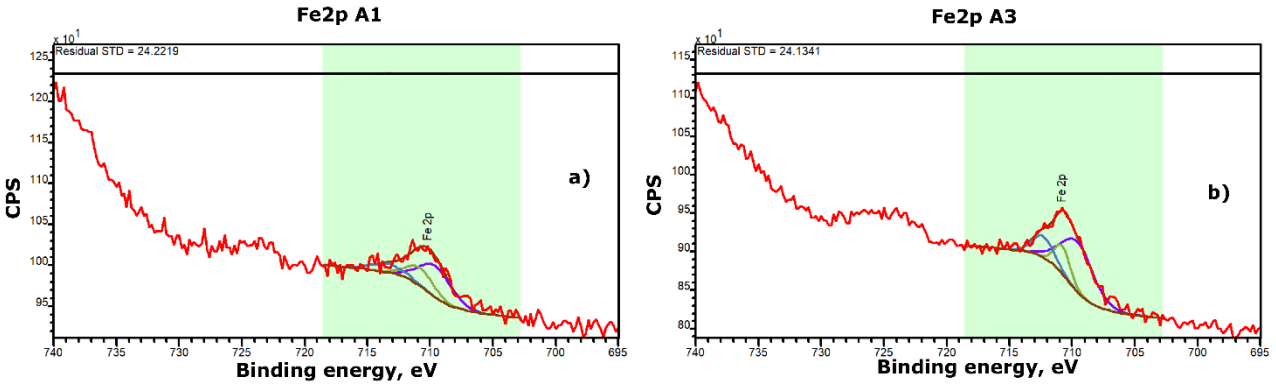

Figure 4.10. XPS detailed core-level spectra in the Fe2p region for A1 (a) and A3 (b) samples, respectively.

4.6 Measurements of Si2p

The XPS detailed core-level spectra in the Si2p region (Figure 4.11) demonstrate Si oxide peak dominance for SiCDCHibBM3, SiCDCHibBM4 and SiCDCHibBM1 samples.

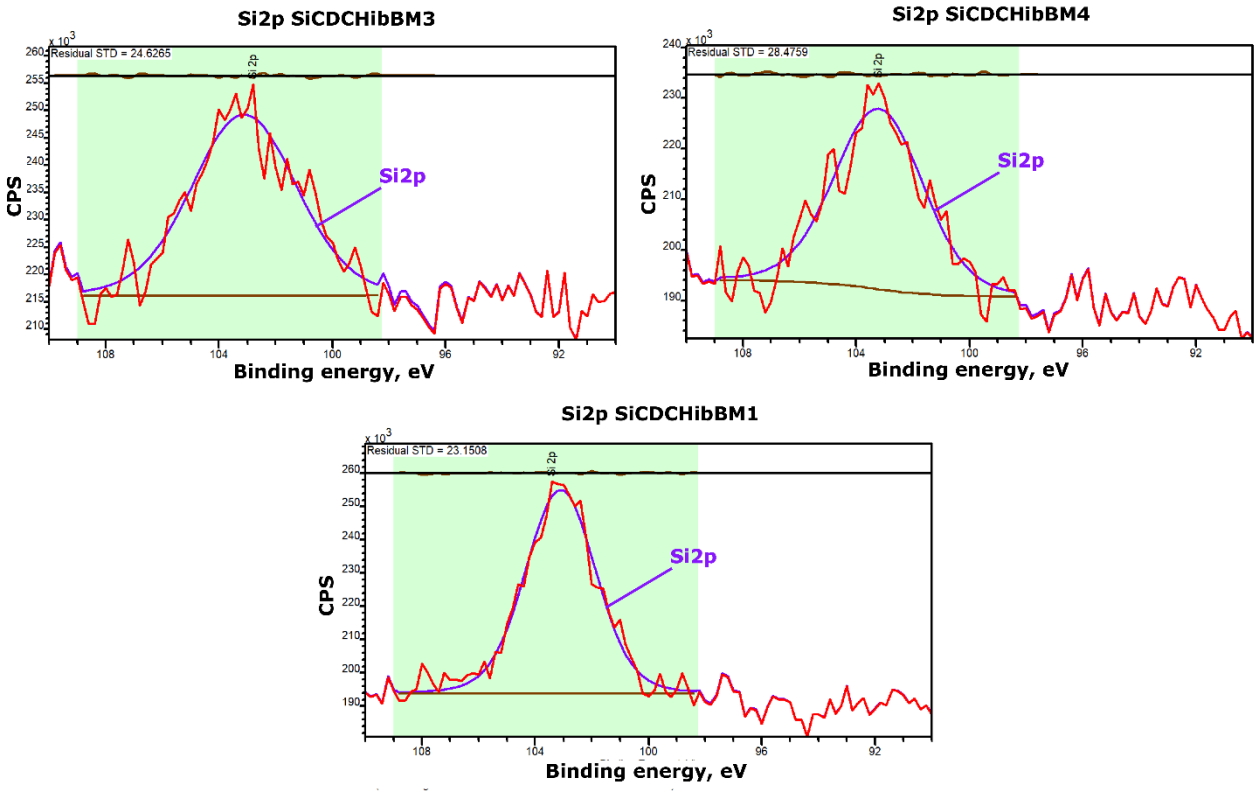

Figure 4.11. XPS detailed core-level spectra in the Si2p region for SiCDCHibBM3 (a), SiCDCHibBM4 (b) and SiCDCHibBM1 (c) samples, respectively.

Table 4.9 describes Si content of catalyst materials from the Si2p spectra.

Table 4.9. Concentration of Si as determined from the Si2p XPS peak for SiCDCHibBM1, SiCDCHibBM3, and SiCDCHibBM4 samples.

Name	Position, eV	Atomic concentration of sample, %
SiCDCHibBM3		
Si 2p	103.1	0.5
SiCDCHibBM4		
Si 2p	103.2	0.5
SiCDCHibBM1		
Si 2p	103.1	0.5

4.7 Measurements of Zr3d

The measured core-level XPS spectra in the Zr3d region were deconvoluted by using two pairs of spin-orbit split ($Zr3d_{3/2}$ and $Zr3d_{5/2}$) photoelectron peaks, thus giving us two oxidized states. However, we suggest that both of these oxidized states are due to ZrO_2 because in earlier XPS studies ZrO_2 has shown very strong local charging effects which may lead to different binding energies in different particles [39]. As these ZrO_2 particles were introduced into samples during ball-milling using ZrO_2 balls, the concentration of ZrO_2 is very low (below 0.2%, see Table 4.2), but these Zr3d peaks are still observable because of their low binding energy lay in the region of the spectrum, where the background is low.

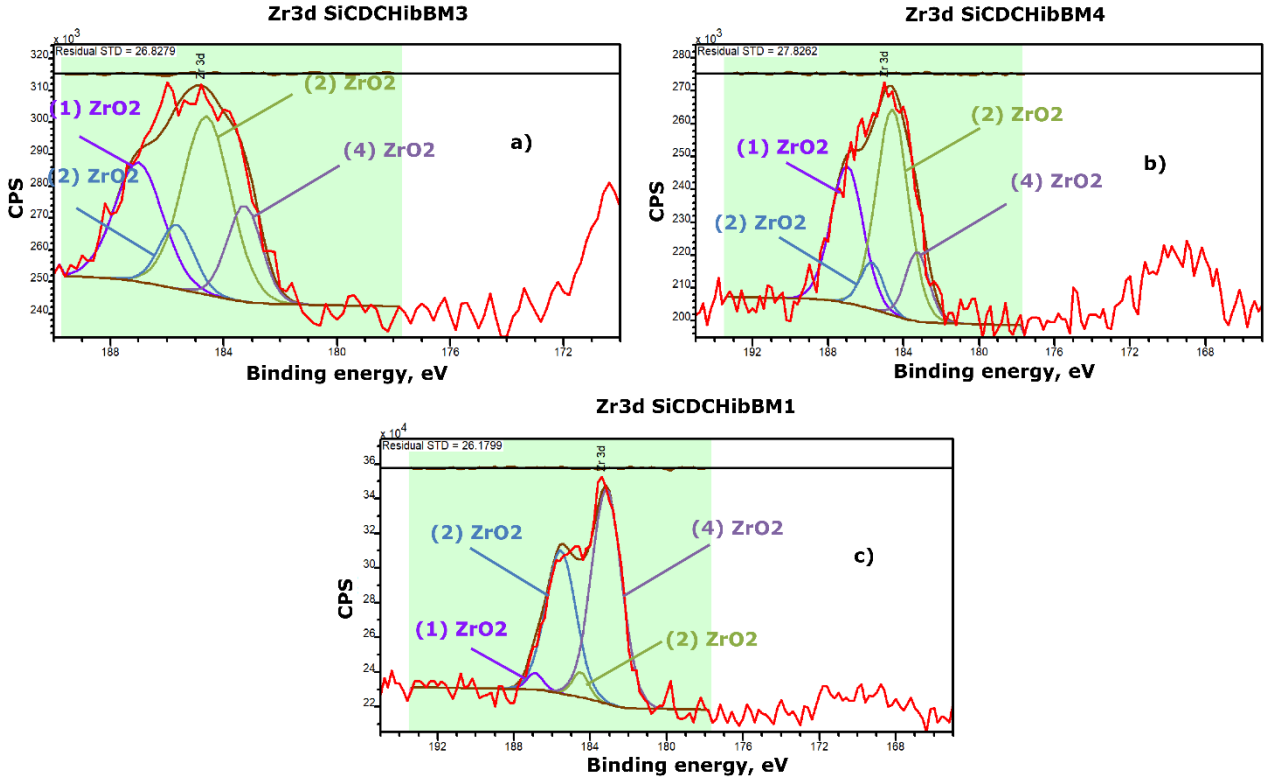

Figure 4.12. XPS detailed core-level spectra in the Zr3d region for SiCDCHibBM3 (a), SiCDCHibBM4 (b) and SiCDCHibBM1 (c) samples, respectively.

SUMMARY

The aim of the study was to determine the surface composition of electrocatalytic materials by X-ray photoelectron spectroscopy (XPS). In this master's thesis, two sets of carbon-based electrocatalysts were analyzed. The first set of samples were metal-nitrogen-carbon (MNC) catalysts (doped with Fe and Co). The effect of acid treatment during preparations on the composition of these catalysts has been studied. The second set of samples consists of carbide-derived carbon (CDC) catalysts, which were ball-milled under different conditions.

XPS was used as an analytical method for the quantification and analysis of material in the topmost layers of the sample. According to the XPS, the main elements in samples are carbon, nitrogen and oxygen. In the first series (MNC-based) also the presence of iron and cobalt, introduced in preparation, was confirmed. In CDC-based electrocatalysts also the presence of silicon and zirconium was observed.

The XPS spectra in the N1s region showed seven different peaks for all investigated samples (*pyridinic-N*, p*yrrolic-N, amines/metal-Nx, imine-N, graphitic-N, NO* and *bulk N-H)*. In samples A1-A4, SiCDCHibBM1 and SiCDCHibBM4 nitrogen was mainly in *pyridinic-N* state.

The quantitative analysis of C1s XPS spectra shows seven peaks (sp^2 *C*, sp^3 *C, C-O-C, C=O, C-O=C,* π-π*, and *carbide*) with significant dominance of sp^2 carbon.

Measurements and assessment of O1s XPS spectra demonstrate different oxygen-containing functional groups on the surface (*metal oxide, O=C-OH carboxyl, C=O carbonyl and C-O, C-OH, chemisorbed O*).

In the case MNC-based catalysts, the comparison of materials treated and untreated with acid during preparation showed that the metal content at the surface was higher for untreated catalysts (A3-Fe and A4-Co), due to the presence of transition metal-containing nanoparticles at the surface.

The study of different carbon-oxygen functionalities, nitrogen species and metal-N_x sites on the catalyst surface was of particular importance. The electrocatalytic properties of catalyst materials towards the oxygen reduction reaction are related to the surface concentration of active species as determined by XPS.

REFERENCES

1. Thomas, C. E. Fuel Cell and Battery Electric Vehicles Compared. *Int. J. Hydrogen Energy* **2009**, *34* (15), 6005–6020. https://doi.org/10.1016/j.ijhydene.2009.06.003.
2. Li, Q.; Wu, G.; Cullen, D. A.; More, K. L.; Mack, N. H.; Chung, H. T.; Zelenay, P. Phosphate-Tolerant Oxygen Reduction Catalysts. *ACS Catal.* **2014**, *4* (9), 3193–3200. https://doi.org/10.1021/cs500807v.
3. Zhang, L.-M.; Wang, Z.-B.; Sui, X.-L.; Li, C.-Z.; Zhao, L.; Gu, D.-M. Nitrogen-Doped Carbon with Mesoporous Structure as High Surface Area Catalyst Support for Methanol Oxidation Reaction. *RSC Adv.* **2016**, *6* (45), 39310–39316. https://doi.org/10.1039/C6RA06104D.
4. Carbide-Derived Carbon/Carbon Nanotube Composite Catalysts Doped with Nitrogen and Transition Metals for Anion Exchange Membrane Fuel Cells. *Meet. Abstr.* **2018**. https://doi.org/10.1149/MA2018-02/45/1544.
5. Watts F.J., Wolstenholme J., An Introduction to Surface Analysis by XPS and AES, Wiley, Chichester, 2003
6. Dicks, A. L. The Role of Carbon in Fuel Cells. *J. Power Sources* **2006**, *156* (2), 128–141. https://doi.org/10.1016/j.jpowsour.2006.02.054.
7. https://xpssimplified.com
8. Seah, M. P.; Dench, W. A. Quantitative Electron Spectroscopy of Surfaces: A Standard Data Base for Electron Inelastic Mean Free Paths in Solids. *Surf. Interface Anal.* **1979**, *1* (1), 2–11. https://doi.org/10.1002/sia.740010103.
9. Hüfner, S. Photoelectron Spectroscopy: Principles and Applications, 3rd ed.; Advanced texts in physics; Springer: Berlin ; New York, 2003.
10. Kabir, S.; Artyushkova, K.; Serov, A.; Kiefer, B.; Atanassov, P. Binding Energy Shifts for Nitrogen-Containing Graphene-Based Electrocatalysts - Experiments and DFT Calculations: Analyzing Structure-Property Relationships of Functionalized Materials. Surf. Interface Anal. 2016, 48 (5), 293–300. https://doi.org/10.1002/sia.5935.
11. Ning, X.; Li, Y.; Ming, J.; Wang, Q.; Wang, H.; Cao, Y.; Peng, F.; Yang, Y.; Yu, H. Electronic Synergism of Pyridinic- and Graphitic-Nitrogen on N-Doped Carbons for the Oxygen Reduction Reaction. Chem. Sci. **2019**, 10 (6), 1589–1596. https://doi.org/10.1039/C8SC04596H.
12. An introduction to the SES-100 analyser, *VG Scienta AB* **2006**.
13. XR3E2 Twin Anode X-Ray – Operating Manual, *Thermo Scientific*.
14. Walton, J. *Peak Fitting with CasaXPS: A Casa Pocket Book*; Acolyte Science: Knutsford, 2011.
15. Shirley, D. A. High-Resolution X-Ray Photoemission Spectrum of the Valence Bands of Gold. *Phys. Rev. B* **1972**, *5* (12), 4709–4714. https://doi.org/10.1103/PhysRevB.5.4709.

APPENDIXES

Appendix 1. Literature assignments of BE of the most common samples.

Literature assignments of BE of the most common samples for C1s.

Reference	Carbide. eV	sp^2. eV	sp^3. eV	C-C. eV	Carbon oxide, eV	C sp^3 - OH, eV	C sp^2 = O, eV	C-O-C, C-OH, eV	C-N, eV	C=O, eV	O-C=O, eV	π- π*, eV	COOH, eV	Subject
[1]		284.3							287.4					Graphene
[2]		284.4	285.1			285.8	286.3							Carbon hybridisation in carbon nanomaterials
[3]					285			287.1	286.2	288			289.4	Oxygen reduction reaction catalyst
[4]				285					286					F-N-C oxygen reduction catalysts
[5]		284	285							288				Ultrathin carbon overcoats
[6]		284.6;	285.2				286.3 C-O/C-N			287.5 C=O/C=N	288.8			Graphene nanoflakes
[7]	282-283.5			285	286 C-O					288-289				Organic polymers

Literature assignments of BE of the components present in electrocatalysts or N1s peaks.

References	Imine. eV	Nitrile. eV	Pyridinic-N. eV	Nx-Fe. eV	Amine. eV	Pyrrolic-N. eV	Hydrogenated N, eV	Graphitic, eV	Bulk-N-H, eV	Quaternary N, eV	Oxydized N, eV	Subject
[8]	397.6		398.3	399.5		400.9		402.1			>403	Oxygen reduction reaction catalyst
[9]			398	399.5			401	402.2		403.2	405	F-N-C oxygen reduction catalysts
[10]	398		398.8	398.8	399.9	400.7	400.7	401.8				Fe−N−C ORR electrocatalysts
[11]	398		398.8	399.8		400.7		403.3		401.8		Nitrogen-containing graphene based catalysts
[12]		398	398.6	399.2-399.5		400.7		403		401.8		Fe-N-C oxygen reduction fuel cell catalyst derived from carbendazim
[13]			398.1			399.9		401			403.3	Cobalt-containing nitrogen-doped carbon aerogels
[14]			397.9	399.5		400.8		402.6			404.8	Graphene oxides
[15]			398.6			400.5				401.3±0.3	402-405	Nanostructured nonprecious metal catalysts
[16]	397.4		383.3	399.4			401	402	403		>403	Low-temperature proton exchange membrane
[17]			398.6			399.9		401.2		401.2	403.1;405.2	Graphene nanoflakes

Literature assignments of BE of the components present in electrocatalysts for O1s peaks.

Articles	Quinones, eV	Carbonyl group (C=O), eV	O=C-OH, eV	Ether (C-O), eV	C-O-C in ester, OH in carbonyl, eV	Carboxylic group (COOH), eV	Water, eV	Subject
[1]		530.6		532	533.4			Assigment of O1s components of the plasma treatment
[18]		531.3					532.9	Carbon-nitride thin films
[2]				531.7	533.2			Carbon hybridisation in carbon nanomaterials
[19]	530.700	531.4		532.4	533.7		535	Tuning the acid/base properties of nanocarb by functionalization via Amination
[20]	530.05 - 530.17	532.05 - 532.21		532.69-533.09	533.56-533.70			Electrochem capacitive behavior of reduced graphene oxides
[21]	531.30				533.3	534.10		Nanostructured carbon catalysts
[22]		530.6		532.3-533.5		534.30	536.3	Activated carbon
[23]				532.5				Characterization of chemical functionalised MWCNTs and SWCNTs
[24]	531.10	532.3					535.9	Activated carbon
[25]		531.6		532.4		533.60	535	Carbon fibres
[26]		531.4-531.6		533		532.30	535.5	Carbon-fibre surface
[17]	530.5 C=O	531.5	533.2 C-O					Graphene nanoflakes

References for appendix

1. Bertóti, I.; Mohai, M.; László, K. Surface Modification of Graphene and Graphite by Nitrogen Plasma: Determination of Chemical State Alterations and Assignments by Quantitative X-Ray Photoelectron Spectroscopy. *Carbon* **2015**, *84*, 185–196. https://doi.org/10.1016/j.carbon.2014.11.056.
2. Lesiak, B.; Kövér, L.; Tóth, J.; Zemek, J.; Jiricek, P.; Kromka, A.; Rangam, N. C Sp2/Sp3 Hybridisations in Carbon Nanomaterials – XPS and (X)AES Study. *Applied Surface Science* **2018**, *452*, 223–231. https://doi.org/10.1016/j.apsusc.2018.04.269.
3. Gokhale, R.; Chen, Y.; Serov, A.; Artyushkova, K.; Atanassov, P. Direct Synthesis of Platinum Group Metal-Free Fe-N-C Catalyst for Oxygen Reduction Reaction in Alkaline Media. *Electrochemistry Communications* **2016**, *72*, 140–143. https://doi.org/10.1016/j.elecom.2016.09.013.
4. Hossen, M. M.; Artyushkova, K.; Atanassov, P.; Serov, A. Synthesis and Characterization of High Performing Fe-N-C Catalyst for Oxygen Reduction Reaction (ORR) in Alkaline Exchange Membrane Fuel Cells. *Journal of Power Sources* **2018**, *375*, 214–221. https://doi.org/10.1016/j.jpowsour.2017.08.036.
5. Chernyak, S. A.; Ivanov, A. S.; Arkhipova, E. A.; Shumyantsev, A. V.; Strokova, N. E.; Maslakov, K. I.; Savilov, S. V.; Lunin, V. V. Mechanism and Kinetics of Decomposition of N-Containing Functional Groups in Few-Layer Graphene Nanoflakes. *Applied Surface Science* **2019**, *484*, 228–236. https://doi.org/10.1016/j.apsusc.2019.04.077.
6. Dwivedi, N.; Yeo, R. J.; Satyanarayana, N.; Kundu, S.; Tripathy, S.; Bhatia, C. S. Understanding the Role of Nitrogen in Plasma-Assisted Surface Modification of Magnetic Recording Media with and without Ultrathin Carbon Overcoats. *Sci Rep* **2015**, *5* (1), 7772. https://doi.org/10.1038/srep07772.
7. Watts, J. F. High Resolution XPS of Organic Polymers: The Scienta ESCA 300 Database. G. Beamson and D. Briggs. 280pp., £65. John Wiley & Sons, Chichester, ISBN 0471 935921, (1992): BOOK REVIEW. *Surf. Interface Anal.* **1993**, *20* (3), 267–267. https://doi.org/10.1002/sia.740200310.
8. Artyushkova, K.; Matanovic, I.; Halevi, B.; Atanassov, P. Oxygen Binding to Active Sites of Fe–N–C ORR Electrocatalysts Observed by Ambient-Pressure XPS. *J. Phys. Chem. C* **2017**, *121* (5), 2836–2843. https://doi.org/10.1021/acs.jpcc.6b11721.
9. Kreek, K.; Sarapuu, A.; Samolberg, L.; Joost, U.; Mikli, V.; Koel, M.; Tammeveski, K. Cobalt-Containing Nitrogen-Doped Carbon Aerogels as Efficient Electrocatalysts for the Oxygen Reduction Reaction. *ChemElectroChem* **2015**, *2* (12), 2079–2088. https://doi.org/10.1002/celc.201500275.

10. Mooste, M.; Kibena-Põldsepp, E.; Vassiljeva, V.; Merisalu, M.; Kook, M.; Treshchalov, A.; Kisand, V.; Uibu, M.; Krumme, A.; Sammelselg, V.; Tammeveski, K. Electrocatalysts for Oxygen Reduction Reaction Based on Electrospun Polyacrylonitrile, Styrene–Acrylonitrile Copolymer and Carbon Nanotube Composite Fibres. *J Mater Sci* **2019**, *54* (17), 11618–11634. https://doi.org/10.1007/s10853-019-03725-z.
11. Wu, G.; Zelenay, P. Nanostructured Nonprecious Metal Catalysts for Oxygen Reduction Reaction. *Acc. Chem. Res.* **2013**, *46* (8), 1878–1889. https://doi.org/10.1021/ar400011z.
12. Artyushkova, K.; Serov, A.; Doan, H.; Danilovic, N.; Capuano, C. B.; Sakamoto, T.; Kishi, H.; Yamaguchi, S.; Mukerjee, S.; Atanassov, P. Application of X-Ray Photoelectron Spectroscopy to Studies of Electrodes in Fuel Cells and Electrolyzers. *Journal of Electron Spectroscopy and Related Phenomena* **2019**, *231*, 127–139. https://doi.org/10.1016/j.elspec.2017.12.006.
13. Arrigo, R.; Hävecker, M.; Wrabetz, S.; Blume, R.; Lerch, M.; McGregor, J.; Parrott, E. P. J.; Zeitler, J. A.; Gladden, L. F.; Knop-Gericke, A.; Schlögl, R.; Su, D. S. Tuning the Acid/Base Properties of Nanocarbons by Functionalization via Amination. *J. Am. Chem. Soc.* **2010**, *132* (28), 9616–9630. https://doi.org/10.1021/ja910169v.
14. Oh, Y. J.; Yoo, J. J.; Kim, Y. I.; Yoon, J. K.; Yoon, H. N.; Kim, J.-H.; Park, S. B. Oxygen Functional Groups and Electrochemical Capacitive Behavior of Incompletely Reduced Graphene Oxides as a Thin-Film Electrode of Supercapacitor. *Electrochimica Acta* **2014**, *116*, 118–128. https://doi.org/10.1016/j.electacta.2013.11.040.
15. Woods, M. P.; Gawade, P.; Tan, B.; Ozkan, U. S. Preferential Oxidation of Carbon Monoxide on Co/CeO2 Nanoparticles. *Applied Catalysis B: Environmental* **2010**, *97* (1–2), 28–35. https://doi.org/10.1016/j.apcatb.2010.03.015.
16. Walczyk, M.; Świątkowski, A.; Pakuła, M.; Biniak, S. Electrochemical Studies of the Interaction between a Modified Activated Carbon Surface and Heavy Metal Ions. *J Appl Electrochem* **2005**, *35* (2), 123–130. https://doi.org/10.1007/s10800-004-2399-0.
17. Okpalugo, T. I. T.; Papakonstantinou, P.; Murphy, H.; McLaughlin, J.; Brown, N. M. D. High Resolution XPS Characterization of Chemical Functionalized MWCNTs and SWCNTs. *Carbon* **2005**, *43* (1), 153–161. https://doi.org/10.1016/j.carbon.2004.08.033.
18. Figueiredo, J. L.; Pereira, M. F. R.; Freitas, M. M. A.; Órfão, J. J. M. Modification of the Surface Chemistry of Activated Carbons. *Carbon* **1999**, *37* (9), 1379–1389. https://doi.org/10.1016/S0008-6223(98)00333-9.
19. Desimoni, E.; Casella, G. I.; Salvi, A. M. XPS/XAES Study of Carbon Fibres during Thermal Annealing under UHV Conditions. *Carbon* **1992**, *30* (4), 521–526. https://doi.org/10.1016/0008-6223(92)90170-2.

20. Azdad, Z.; Marot, L.; Moser, L.; Steiner, R.; Meyer, E. Valence Band Behaviour of Zirconium Oxide, Photoelectron and Auger Spectroscopy Study. *Sci Rep* **2018**, *8* (1), 16251. https://doi.org/10.1038/s41598-018-34570-w.
21. Kabir, S.; Artyushkova, K.; Serov, A.; Kiefer, B.; Atanassov, P. Binding Energy Shifts for Nitrogen-Containing Graphene-Based Electrocatalysts - Experiments and DFT Calculations: Analyzing Structure-Property Relationships of Functionalized Materials. Surf. Interface Anal. 2016, 48 (5), 293–300. https://doi.org/10.1002/sia.5935.
22. Hüfner, S. Photoelectron Spectroscopy: Principles and Applications, 3rd ed.; Advanced texts in physics; Springer: Berlin ; New York, 2003.
23. Ning, X.; Li, Y.; Ming, J.; Wang, Q.; Wang, H.; Cao, Y.; Peng, F.; Yang, Y.; Yu, H. Electronic Synergism of Pyridinic- and Graphitic-Nitrogen on N-Doped Carbons for the Oxygen Reduction Reaction. Chem. Sci. **2019**, 10 (6), 1589–1596. https://doi.org/10.1039/C8SC04596H.

Non-exclusive licence to reproduce thesis and make thesis public

I, Dmytro Danilian,

(*author's name*)

1. herewith grant the University of Tartu a free permit (non-exclusive licence) to

reproduce, for the purpose of preservation, including for adding to the DSpace digital archives until the expiry of the term of copyright,

X-Ray Photoelectron Spectroscopy Studies of Carbon Based Electrocatalytic Materials,
(title of thesis)

supervised by Arvo Kikas, Vambola Kisand, Kaido Tammeveski.

(supervisor's name)

2. I grant the University of Tartu a permit to make the work specified in p. 1 available to the public via the web environment of the University of Tartu, including via the DSpace digital archives, under the Creative Commons licence CC BY NC ND 3.0, which allows, by giving appropriate credit to the author, to reproduce, distribute the work and communicate it to the public, and prohibits the creation of derivative works and any commercial use of the work until the expiry of the term of copyright.

3. I am aware of the fact that the author retains the rights specified in p. 1 and 2.

4. I certify that granting the non-exclusive licence does not infringe other persons' intellectual property rights or rights arising from the personal data protection legislation.

Dmytro Danilian

22/05/2020

X-Ray Photoelectron Spectroscopy Studies of Carbon-Based Electrocatalytic Materials

X-ray photoelectron spectroscopy (XPS) was used for investigation of carbon-based electrocatalysts. According to the measurements, in a majority of samples, the main components were carbon, nitrogen and oxygen, as expected. In metal-nitrogen-carbon catalysts, the presence of iron and cobalt, introduced during preparation, was proved and in carbide-derived carbon catalysts zirconium and silicon were found. The results of N1s measurements showed 7 different nitrogen species in samples such as *pyridinic-N, pyrrolic-N, amines/metal-Nx, imine-N, graphitic-N, NO* and *bulk N-H*. The quantitative analysis of C1s demonstrated 7 states of carbon (sp^2 *C,* sp^3 *C, C-O-C, C=O, C-O=C,* π-π*, and *carbide*) with significant dominance of sp^2 carbon. In O1s spectrum the following different oxygen-containing groups were observed: *metal oxide, O=C-OH carboxyl, C=O carbonyl, C-O, C-OH,* and *chemisorbed O*. The chemical composition of the samples was determined.

The study of different carbon-oxygen functionalities and nitrogen species on the catalyst surface was of particular importance. The electrocatalytic properties of the catalyst material for the oxygen reduction reaction are related to the active sites on the catalyst surface. Determined peaks agree, in general, well with literature findings in different electrocatalysts.

Keywords: X-ray photoelectron spectroscopy, Electrocatalyst, Fuel cell.

CERC code: P352

Süsinikupõhiste elektrokatalüütiliste materjalide fotoelektronspektroskoopilised uuringud

Süsinikupõhiste elektrokatalüütiliste materjalide uurimiseks kasutati röntgenfotoelektron-spektroskoopiat. Mõõtmiste kohaselt koosnevad kõik proovid ootuspäraselt peamiselt süsinikust, lämmastikust ja hapnikust. Metall-lämmastik-süsinik katalüsaatormaterjalide korral näidati nende valmistamise käigus sisse viidud raua ja koobalti olemasolu, karbiidset päritolu süsinikust valmistatud proovides leiti tsirkooniumi ja räni olemasolu. Lämmastiku 1s mõõtmiste tulemused näitasid kõigis uuritud proovides 7 erineva lämmastikuvormi olemasolu: püridiinne-N, pürroolne-N, amiinid/metall-Nx, imiin-N, grafiitne-N, NO ja N-H. Süsiniku 1s fotoelektronspektrid näitasid erinevate süsinikuvormide olemasolu: (sp^2 C, sp^3 C, C-O-C, C=O, C-O=C, π-π * ja karbiid), kusjuures sp^2 süsinik domineeris. Hapniku korral tuvastati järgmised erinevad funktsionaalsed rühmad: metalloksiid, O=C-OH (karboksüül), C=O (karbonüül ja CO), C-OH ja absorbeerunud O. Määrati kõigi katalüsaatormaterjalide pinna keemiline koostis.

Katalüsaatormaterjalide elektrokatalüütilised omadused hapniku redutseerimisel on seotud aktiivsete tsentritega materjalide pinnal. Seetõttu on erinevate süsiniku-hapniku ja lämmastikurühmade tuvastamine katalüsaatori pinnal eriti oluline. Saadud tulemused on üldiselt heas kooskõlas kirjanduses toodud andmetega.

Märksõnad: Röntgenfotoelektronspektroskoopia, elektrokatalüsaator, kütuseelement.